Cells Tissues Organs

Cells Tissues Organs 2008;187:59–84
DOI: 10.1159/000109964

Published online: December 11, 2007

Biomechanics of the Bat Limb Skeleton: Scaling, Material Properties and Mechanics

Sharon M. Swartz[a, b] Kevin M. Middleton[a, c]

[a]Department of Ecology and Evolutionary Biology and [b]Division of Engineering, Brown University, Providence, R.I., [c]Department of Biology, California State University, San Bernardino, Calif., USA

Key Words
Biomechanics · Bone · Allometry · Chiroptera · Bats

Abstract
Background/Aims: Wing skeletons of bats are uniquely specialized for flight, reflecting both evolutionary history and the need to maintain structural integrity while generating aerodynamic forces. ***Methods:*** We analyzed the anatomical structure of bat wing skeletons in the context of scaling patterns relative to other mammals, material properties and the mechanical function of the wing bones during flight. ***Results:*** Compared with nonvolant mammals, the bones of the bat forelimb are elongated, even after correcting for shared phylogenetic history. Bats have consistently larger-diameter bones in the forelimb than do nonvolant mammals but significantly narrower hindlimb bones. Mineralization in the cortical bone of wings is lower than in the long bones of other adult mammals, with a proximodistal gradient of decreasing mineralization. The distal phalanges have only a small amount of mineralized tissue underlying the articular cartilage. Loads required to elicit a 10% length deflection in the wing bones of *Glossophaga soricina* varied approximately 50-fold along the wing and flexural stiffness nearly 200-fold. Commensurate with low mineralization and flexural stiffness, bat bones experience extraordinarily high bending strains during flight. ***Conclusion:*** Bat limb skeletons share features with other mammals and possess specialized characteristics, mostly related to the mechanical demands of flight.

Abbreviations used in this paper

AIC	Akaike information criterion
BMP	bone morphogenetic protein
EI	flexural stiffness
GLS	generalized least squares
ln ML	natural logarithm of maximum likelihood
MC	metacarpal
OLS	ordinary least squares
OU REG	Ornstein-Uhlenbeck model of regression
pFDR	positive false discovery rate
RMA	reduced major axis

Introduction

The limb skeletons of bats show unmistakable signatures of the evolutionary journey from typical quadrupedal mammals to highly derived flight specialists. Indeed, it takes no anatomical or biomechanical training to infer specialization for flight from the skeleton of a bat; it is a challenge to even imagine another primary function for the greatly elongated digits of the bat hand. Within this broad pattern, however, there are numerous subtle specializations of the bat limb skeleton that appear to relate to the mechanics of flight. These distinctive features can be found at several scales of investigation, from the whole

KARGER
Fax +41 61 306 12 34
E-Mail karger@karger.ch
www.karger.com

1422–6405/08/1871–0059$24.50/0

Accessible online at:
www.karger.com/cto

Dr. Sharon Swartz
Department of Ecology and Evolutionary Biology
Box G-B206, Brown University
Providence, RI 02912 (USA)
Tel. +1 401 863 1582, Fax +1 401 863 7544, E-Mail sharon_swartz@brown.edu

skeleton, through organs, macroscopic organ features, cells and even finer-scale variation. Technological advances in the study of mechanical functioning of biological tissues at ever finer scales hold much promise, and it is likely that we will soon be able to probe design and mechanical function of wing tissues, particularly bone, skin and tendon at levels down to the nanoscale. As researchers seek evidence of bats' distinctive adaptation to the demands of flight in new ways, it is most appropriate to review and synthesize some of the relevant work of the last 20 years.

Here, we bring together diverse kinds of information relating to mechanical function to provide an integrated view of the structural design of bat wing bones. We review the relevant literature, provide new analyses and employ the perspective of this overview to suggest new research directions that are likely to prove fruitful. We focus particularly on three distinct forms of analysis. First, we evaluate the body-size-associated patterns of scaling of whole-bone geometry in the bat limb. We base our discussion on published work [Swartz, 1997], but also reanalyze these data from explicitly phylogenetic perspectives [Felsenstein, 1985; Harvey and Pagel, 1991; Garland et al., 1992]. We use this more rigorous phylogenetically based analysis to illuminate evolutionary patterning in the limb skeleton of bats and their nonvolant relatives. Second, building on the previous work of Papadimitriou et al. [1996], we appraise the variation in mechanical characteristics of the tissue of the wing bones and discuss implications of these features for the mechanics and aerodynamics of bat flight. Third, we describe the net loading regimes imposed by flight on the bones of the bat wing as characterized by in vivo strain gauge analysis, and use the results of new and previously reported strain analysis [Swartz et al., 1992] to help provide the appropriate performance context for analyses of bone geometry and materials. Finally, we identify questions that have yet to be fully addressed by the research community, and propose possible approaches to tackle some of these unanswered questions.

Materials and Methods

Limb Bone Allometry

Measurements were collected directly from specimens or radiographs of specimens housed at the United States National Museum, Smithsonian Institution (Washington, D.C., USA), American Museum of Natural History (New York, N.Y., USA), British Museum of Natural History (London, UK), Queensland Museum (Brisbane, Australia) and the Australian Museum (Sydney, Australia). Additional comparative data were derived from the literature [Kurian, 1993; Chickering, 1995].

We measured both fore- [humerus, radius, metacarpals (MCs) III and V, proximal phalanges III and V, middle phalanx III, and distal phalanges III and V] and hindlimb elements (femur and tibia). Where possible, we measured length and 2 orthogonal midshaft diameters from each bone (online suppl. appendix 1, www.karger.com/doi/10.1159/000109964). All data were $\log_{10}$ transformed prior to analysis.

The taxonomic sampling included 271 species of bats and nonvolant mammals (table 1). All major clades of bats were sampled (136 species total), whereas disproportionately large numbers of primates and rodents were included in the nonvolant mammal sample, in addition to small-bodied marsupials, insectivores, dermopterans, elephant shrews, hyraxes, carnivores and artiodactyls (135 species total). The mass range covered approximately 5 orders of magnitude from the smallest (3.1 g; *Thyroptera discifera*) to the largest (169,750 g; *Gorilla gorilla*). Some species are represented by single individuals, whereas other measurements are means from multiple individuals. For species with pronounced sexual size dimorphism, males and females were included as distinct 'taxa'. Body masses were derived from the literature [Eisenberg, 1981, 1989; Nowak, 1991; Silva and Downing, 1995]. Data were saved as a .tip file for regression (see below; online suppl. appendix 2, www.karger.com/doi/10.1159/000109964).

Phylogeny

A phylogenetic tree including all 271 species was constructed, based on published phylogenetic hypotheses, using Mesquite software (version 1.12 [Maddison and Maddison, 2006]; http://mesquiteproject.org; fig. 1). Our approach used both higher-level phylogenies [Murphy et al., 2001] to determine the overall tree structure and family- or genus-level phylogenetic hypotheses to determine interrelationships at lower taxonomic levels (family, genus, species). The full list of tree sources is provided in online supplement appendix 2 (www.karger.com/doi/10.1159/000109964). Nodes that could not be resolved or for which published phylogenetic hypotheses were uncertain were treated as polytomies. Branch lengths were scaled arbitrarily according to the method proposed by Pagel [1992]. The phylogenetic tree was exported from Mesquite as a .pdi file [Garland et al., 1999; Garland and Ives, 2000] and converted to a phylogenetic distance matrix using the DOS program PDDIST [Garland et al., 1993]. This distance matrix, representing the tree scaled according to Pagel's arbitrary branch length method [Pagel, 1992], served as the base set of branch lengths for phylogenetic regression (see below). The original Mesquite nexus file (.nex) and distance matrix file (.dsc) are available in online supplement appendix 3 (www.karger.com/doi/10.1159/000109964).

Regression Analysis

We studied the scaling of each skeletal variable versus body mass with phylogenetic grouping (bat/nonvolant mammal) as a covariate. Using the Matlab (version 7.4.0 R2007a; MathWorks Inc.) program Regression.V.2 [Garland and Ives, pers. commun.], three regression models were compared for each variable: (1) ordinary least squares (OLS) regression, (2) phylogenetic generalized least squares (GLS) regression using Pagel's method of assigning arbitrary branch lengths (Pagel GLS) [Pagel, 1992], and (3) GLS phylogenetic regression using branch lengths scaled according to a parameter deter-

Table 1. Taxa included in analysis of skeletal allometry

Chiroptera
Emballonuridae
Balantiopteryx plicata
Coleura afra
Cormura brevirostrus
Diclidurus albus
Diclidurus ingens
Diclidurus isabellus
Emballonura monticola
Emballonura alecto
Peropteryx kappleri
Peropteryx macrotis
Rhynchonycteris naso
Saccopteryx bilineata
Taphozous longimanus
Taphozous melanopogon
Taphozous solifer
Megadermatidae
Macroderma gigas
Megaderma lasiae
Megaderma spasma
Molossidae
Chaerephon plicata
Cheiromeles torquatus
Molossops cerastes
Molossus ater
Molossus nigricans
Mops leucostigma
Otomops martiensseni
Tadarida aegyptiaca
Tadarida brasiliensis
Tadarida condylura
Tadarida leucostigma
Tadarida yucatanica
Momoopidae
Mormoops megalophylla
Pteranotus gymnonotus
Pteranotus davyi
Pteronotus parnellii
Pteronotus rubiginosa
Mystacinidae
Mystacina tuberculata
Natalidae
Natalus stramineus
Natalus tumidirostris
Noctilionidae
Noctilio leporinus
Noctilio labialis
Nycteridae
Nycteris arge
Nycteris grandis
Nycteris hispida
Nycteris macrotis
Nycteris thebaica
Phyllostomidae
Anoura cultrata
Artibeus jamaicensis
Artibeus lituratus
Artibeus obscurus
Artibeus toltecus
Artibeus watsoni
Carollia brevicauda
Carollia castanea
Carollia perspicillata
Centurio senex
Chiroderma salvini
Chiroderma villosum
Choeroniscus minor
Choeronycterus mexicanus
Chrotopterus auritus
Desmodus rotundus
Diaemus youngi
Erophylla sezekorni
Glossophaga longirostris
Glossophaga soricina
Leptonycterus sanborni
Lonchophylla robusta
Macrotus mexicanum
Micronycteris megalotis
Micronycteris brachyotis
Mimon benetti
Monophyllus redmani
Natalus stramineus
Natalus tumidirostris
Phyllostomus elongatus
Phyllostomus hastatus
Rhinophylla pumilio
Sturnira lilium
Sturnira ludovicii
Sturnira tildae
Trachops cirrhosus
Uroderma bilobatum
Vampyrodes caraccioli
Vampyrops helleri
Vampyrops vittatus
Vampyrum spectrum
Pteropodidae
Aceradon jubatus
Cynopterus brachyotis
Dobsonia viridis
Dobsonia crenulata
Eidolon helvum
Epomophorus gambianus
Epomophorus wahlbergi
Macroglossus minimus
Myonycteris torquata
Pteropus giganteus
Pteropus mariannus
Pteropus ornatus
Pteropus poliocephalus
Pteropus vampyrus
Rousettus amplexicaudatus
Rousettus aegyptiacus
Rhinolophidae
Hipposideros caffer
Hipposideros commersoni
Hipposideros diadema
Rhinolophus clivosus
Rhinolophus euryale
Rhinolophus ferrumequinum
Rhinolophus stheno
Rhinopomatidae
Rhinopoma muscatellum
Rhinopoma microphyllum
Thyropteridae
Thyroptera tricolor
Thyroptera discifera
Vespertilionidae
Antrozous dubiaquercus
Antrozous pallidus
Barbastella barbastellus
Chalinolobus tuberculatus
Eptesicus brasiliensis
Eptesicus fuscus
Eptesicus pumilus
Glauconycteris poensis
Idionycteris phyllotis
Lasionycteris noctivagans
Lasiurus borealis
Lasiurus castaneus
Lasiurus cinereus
Lasiurus seminolus
Miniopterus escholtzii
Miniopterus schreibersi
Myotis auriculus
Myotis austroriparius
Myotis emarginatus
Myotis grisescens
Myotis lucifugus
Myotis myotis
Myotis nigricans
Myotis thysanodes
Myotis velifer
Myotis volops
Myotis yumanensis
Nyctalus noctula
Nycticeius humeralis
Nyctophilus timoriensis
Philetor brachypterus
Pipistrellus kuhli
Pipstrellus hesperus
Pipstrellus subflavus
Plecotus auritus
Plecotus rafinesquii
Plecotus townsendii
Rhogeessa tumida
Scotoecus hirundo
Scotophilus dinganii
Scotophilus kuhlii
Scotophilus heathi
Tylonycteris robustula

Artiodactyla
Tragulidae
Tragulus javanicus

Carnivora
Canidae
Canis aureus
Otocyon megalotis
Felidae
Felis silvestris
Viverridae
Viverra zibetha

Dasyuromorphia
Dasyuridae
Antechinus stuartii
Sarcophilus laniaris
Sminthopsis leucopus

Dermoptera
Cynocephalidae
Cynocephalus volans
Cynocephalus variegatus

Diprotodontia
Petauridae
Dactylopsila palpator
Petauroides volans
Petaurus australis
Petaurus norfolcensis
Petaurus breviceps
Pseudocheiridae
Hemibelideus lemuroides
Pseudocheirus forbesi
Pseudocheirus herbertensis
Pseudocheirus peregrinus
Pseudocheirus archeri

Hyracoidea
Procaviidae
Procavia capensis

Insectivora
Erinaceidae
Hylomys suillus
Soricidae
Crocidura fuliginosa
Cryptotis parva
Sorex cinereus
Sorex minutus
Suncus murinus
Tenrecidae
Sylvisorex megalura
Microgale cowani

Table 1 (continued)

Macroscelidea
Macroscelididae
Rhynchocyon cirnei

Paramelamorphia
Paramelidae
Perameles bougainville

Primates
Callitrichidae
Callithrix jacchus
Leontopithecus rosalia
Saguinus fuscicollis
Cebidae
Alouatta palliata
Alouatta seniculus
Ateles geoffroyi
Cebus apella
Saimiri sciureus
Cercopithecidae
Cercopithecus mitis
Colobus guereza
Macaca fascicularis
Nasalis larvatus
Papio hamadryas
Presbytis rubicunda
Cheirogaleidae
Cheirogaleus major
Microcebus murinus
Daubentoniidae
Daubentonia madagascarensis
Galagonidae
Euoticus elegantulus
Galago moholi
Galago senegalensis
Galagoides demidoff
Hominidae
Gorilla gorilla
Pan paniscus
Pan troglodytes
Pongo pygmaeus
Hylobatidae
Hylobates lar
Hylobates syndactylus
Indriidae
Propithecus verreauxi
Lemuridae
Avahi laniger
Hapalemur griseus
Lemur fulvus
Varecia variegata
Loridae
Arctocebus calabarensis
Loris tardigradus
Nycticebus coucang
Perodicticus potto
Megaladapidae
Lepilemur edwardsi
Tarsiidae
Tarsius syrichta

Rodentia
Anamaluridae
Anomalurus beecrofti
Anomalurus derbianus
Anomalurus pelii
Anomalurus pusillus
Dasyproctidae
Myoprocta acouchi
Muridae
Acomys russatus
Aethomys kaiseri
Akodon aerosus
Baiomys taylori
Brachyuromys betsileonensis
Clethrionomys gapperi
Lemniscomys griselda
Maxomys alticola
Melanomys caliginosus
Meriones crassus
Microtus mexicanus
Microtus pennsylvanicus
Mus musculus
Neotoma cinerea
Oligoryzomys fulvescens
Pachyuromys duprasi
Peromyscus leucopus
Phyllotis haggardi
Rattus norvegicus
Rattus rattus
Rhabdomys pumilio
Sekeetamys calurus
Sigmodon hipsidus
Thomasomys paramorum
Pedetidae
Pedetes capensis
Sciuridae
Aeromys tephromelas
Aeromys thomasi
Ammospermophilus leucurus
Callosciurus finlaysoni
Callosciurus prevostii
Cynomys gunnisoni
Cynomys ludovicianus
Funambulus pennantii
Funisciurus isabella
Funisciurus pyrropus
Glaucomys sabrinus
Glaucomys volans
Heliosciurus rufobrachium
Hylopetes fimbriatus
Hylopetes phayrei
Marmota bobak
Marmota flaviventris
Marmota monax
Paraxerus cepapi
Petaurista alborufus
Petaurista elegans
Petaurista leucogenys
Petaurista petaurista
Petaurista philippensis
Prosciurillus murinus
Protoxerus stangeri
Ratufa bicolor
Ratufa indica
Rubrisciurus rubriventer
Sciurus carolinensis
Sciurus niger
Sciurus variegatoides
Spermophilus columbianus
Spermophilus elegans
Spermophilus parryi
Spermophilus richardsonii
Spermophilus tridecemlineatus
Spermophilus variegatus
Sundasciurus lowii
Tamias striatus
Tamias umbrinus
Tamiasciurus hudsonicus
Trogopterus xanthipes
Xerus capensis

mined under an Ornstein-Uhlenbeck model of evolution (OU REG). OLS regression assumes that all data points are independent and that residuals are normally distributed with a mean of zero; this is equivalent to phylogenetic regression using a 'star' phylogeny, in which all taxa branch from a single unresolved polytomy [Garland et al., 1999]. At the opposite extreme of incorporating possible hierarchical branching structure is GLS regression using the original tree matrix, scaled to arbitrary branch lengths.

The optimal fit of the distribution of tip data to a phylogenetic tree may come from arbitrary branch lengths, scaled branch lengths or neither. To test the fit of transformed branch lengths using a maximum likelihood estimation, we use the transformation implementation of Blomberg et al. [2003], based on the Ornstein-Uhlenbeck model of stabilizing selection of Brownian motion evolution [Felsenstein, 1988a, b, c; Garland et al., 1993; Hansen and Martins, 1996; Martins et al., 2002; Martins and Housworth, 2002; Butler and King, 2004].

For each model fit, Regression.V.2 returns both main and interaction effects, as well as *t* and *F* statistics for overall interaction differences and individual parameter comparisons, for both main and interaction effects. In addition to computing a regression slope, this method computes an optimal transformation parameter, *d*, which typically falls between 0 (no phylogenetic hierarchy, or star phylogeny) and 1 (branch lengths and taxonomic nesting preserved). In some cases, however, *d* can exceed 1. Diagnostic criteria, including the natural logarithm of the maximum likelihood (ln ML) and the Akaike information criterion (AIC) [Akaike, 1974], are returned, allowing the three models to be compared. AIC can be calculated in several ways; here, we employ

$$\mathrm{AIC} = (-2 \times \ln \mathrm{ML}) + (2 \times \text{number of parameters}).$$

In this way, more complicated models are penalized, and a smaller AIC indicates a better fit. An AIC difference of 4 is suggestive of strong support for a model [Burnham and Anderson, 2002]. Although the ln ML of a model can be used to test for significant differences between nested models via likelihood ratio tests, we focus on AIC.

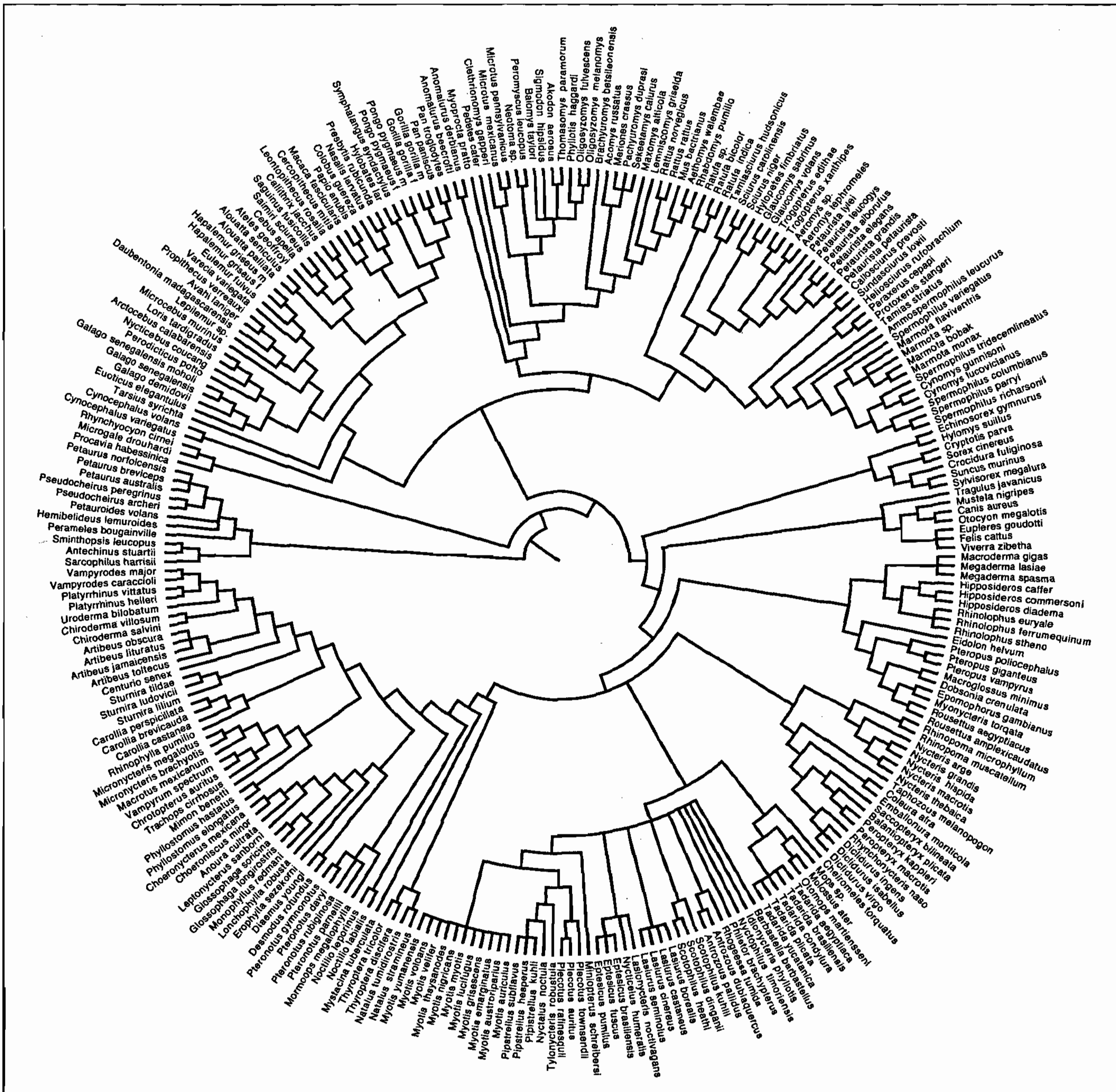

Fig. 1. Phylogenetic tree of 271 species of bats and nonvolant mammals. The phylogenetic relationships of the taxa included were drawn from many sources (see online supplement appendices, www.karger.com/doi/10.1159/000109964), and branch lengths were scaled arbitrarily using the method of Pagel [1992]. Tree drawn using FigTree v. 1.0 (http://evolve.zoo.ox.ac.uk/software.html?id=figtree).

Because of the potential for unknown error in measurements of both body and mass skeletal dimensions, and because we seek to understand allometric patterns and not to develop statistical predictors of bone dimensions per se, we employ reduced major axis (RMA) regression [Rayner, 1985; La Barbera, 1989; Warton et al., 2006; 'standardized major axis' using the terminology of Garland et al., 1992; Warton et al., 2006], particularly given that both phylogenetic information and measurement error are sources of variation in estimation of dependent and independent variables [Ives et al., 2007]. Calculation of the slope of the RMA from

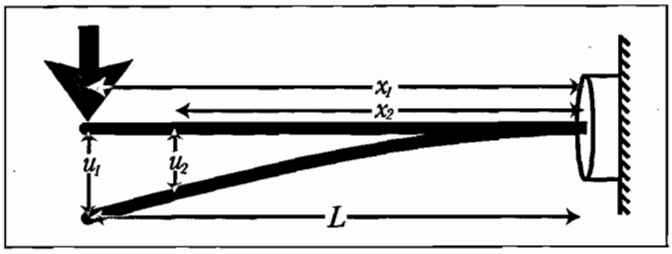

Fig. 2. Schematic drawing of bat bone bending experiments. The bone is fixed at its proximal end (on the right) and free at its distal end at which the load, *P*, is applied (total length = L). Two positions are shown, the predeflection position where the bone is straight, and the position at maximal deflection. In this second position, we record a series of vertical deflections (*e.g.* u_1, u_2) at x positions (x_1, x_2).

OLS regression is accomplished by simply dividing the slope by the correlation coefficient, *r*, the square root of the coefficient of determination, r^2. The calculation of regression slopes is similar for phylogenetic regression methods, including independent contrasts and GLS, except that the coefficient of determination is calculated for a line passing through the origin [Garland et al., 1992; Warton et al., 2006]. In either case, RMA is likely a better estimate of the functional relationship between the trait of interest and body mass, and we present RMA regression coefficients along with those from conventional GLS regressions.

Multiple Comparisons

To control for an increased type I error rate when performing many statistical tests on related sets of data [Rice, 1989], we used the positive false discovery rate (pFDR) method [Storey, 2002; Storey and Tibshirani, 2003]. This test is similar to the familiar Bonferroni correction, sequential Bonferroni correction [Rice, 1989] and the false discovery rate test [Benjamini and Hochberg, 1995; for additional details on these tests, see Curran-Everett, 2000]. Rather than assuming that all null hypotheses are true, and thus that any rejection of the null hypothesis is potentially erroneous, pFDR seeks to estimate the rate of true null hypotheses (p_0), while still controlling the overall type I error rate at the desired level (e.g. family-wise error rate = 0.05). This method assumes that, in comparing two groups, there are some real, true differences and seeks to find a balance between correct and erroneous rejections of the null hypothesis. A pFDR of 0.05 means that 5% of p values that reject the null hypothesis are expected to be false 'positives'. We analyzed the 47 p values from our regression analysis (see Results: Limb Bone Allometry), using the qvalue package [Storey, 2002] for R (version 2.5.0; R Core Development Team, 2007; http://r-project.org). For this sample, with pFDR = 0.05 π_0, the ratio of true null tests to total tests was estimated at 0.67 (i.e. 67% as opposed to 100%, for example in the Bonferroni correction). Based on these results, the four largest p values less than 0.05 could be considered erroneous rejections of the null hypothesis.

Mechanical Properties of Bone Tissue

Ash Content Analysis

We assessed variation among wing bones and across ontogeny in detail in one bat species, *Tadarida brasiliensis* [Papadimitriou et al., 1996]. We analyzed ash content from 33 juveniles, ranging from 1 to 42 days of age, and 5 adults collected during the summers of 1987 and 1988 at Eckert James River Cave, Mason County, Tex., USA, as part of a study on postnatal growth and development [Kunz and Robson, 1995]. Each animal was weighed, frozen, and later dissected, at which time all surrounding soft tissue and marrow were removed from the bones. We employed acetone baths to defat the bones, and then dried them to constant weight. Each element was weighed to the nearest 1.0 mg, then placed in a ceramic crucible for treatment in a muffle furnace to burn away all organic constituents (Sybron Thermolyne 1400 muffle furnace at 600°C for 24 h [Carrier, 1983; Bohr and Schaadt, 1985]). We dried the inorganic remains of each bone overnight at 60°C before measuring the final ash mass, then calculated bone mineral content or ash fraction as the ratio of the mass of the mineral phase of the bone to the mass of dry bone [Cowin, 1989]:

$$\text{mineral content} = (\text{ash mass}/\text{dry mass}) \times 100\%.$$

We used ANOVA to compare the degree of mineralization among bony elements and among age groups, and, for significant differences among groups, the post hoc Scheffé F test to determine where these differences occurred. We employed least squares linear regression analysis to determine the relationship between mineralization and age; the high correlation coefficients in these regressions were not significantly improved with nonlinear regressions or transformations. We compared regression slopes with ANCOVA regression.

Histology

We prepared histological sections of the undemineralized third distal phalanges of the left wings of 3 adult *T. brasiliensis* after finding that ash values were indistinguishable from zero using the protocol described above. Both longitudinal and transverse sections were cut to 50 μm and were stained with Masson's trichrome, which stains collagen blue-green, cytoplasm pink to red and nuclei black, and the von Kossa method, which stains phosphate black. Because the phosphate in bone is largely sequestered in the form of hydroxyapatite, a form of calcium phosphate, this protocol allows the qualitative detection and localization of bone mineralization at levels far lower than those detectable using measurements of ash content [Page, 1982; Schenk et al., 1984].

Whole-Bone Bending

Eleven bones from 1 adult female *Glossophaga soricina* were dissected free of the surrounding wing membrane tissue. Digital calipers were used to measure the length and diameters (anteroposterior and dorsoventral) to the nearest 0.01 mm. The proximal end of each bone was potted in low-melt metal alloy (Small Parts Inc., Miami Lakes, Fla., USA), and, to maintain orientation, the dorsal aspect of the bone was marked. Bones were stored at –20°C frozen in 0.9% saline until tested. Bones were tested in cantilever bending using an Instron 4442 materials testing apparatus (Instron Corp., Norwood, Mass., USA). While the proximal end of the bone was fixed in the potting material, and the distal end was deflected by a 5-newton load cell (fig. 2), which simultaneously recorded the reaction force from the bone at 20 Hz. Individual bones were bent to a deflection of no more than 10% of their total free length. Simultaneously, the entire loading and unloading cy-

cles were videographed. From the digital video, deflection at 5 points along the bone (20, 40, 60, 80 and 100% of free length) was measured using NIH ImageJ (version 1.37v; http://rsb.info.nih.gov/ij/).

To estimate flexural stiffness (*EI*; Young's modulus × second moment of inertia) for these bones, we used the Bernoulli-Euler bending equation:

$$\frac{d^2u}{dx^2} = \frac{P(L-x)}{E \cdot I} \quad (1)$$

where u is the vertical displacement at position x along a beam of total length L, and P is the amount of reaction force for a given u. This equation can be integrated twice and rearranged to give u''/P as a function of L, x and EI:

$$\frac{u''}{P} = \frac{(L-x)}{E \cdot I} \quad (2)$$

EI was modeled as a linearly varying function of x:

$$EI(x) = A + Bx. \quad (3)$$

Optimal values for A and B were determined iteratively using the solver function of Microsoft Excel. Briefly, starting estimates for A and B were input, from which an estimate of $EI(x)$ for the length of the bone, L, was made. For each x position where u and P were measured, the expected value of u/P, deflection per unit load, was calculated by double trapezoidal integration of equation 2. This value was compared to the actual, measured value of u/P to calculate the error, the difference between observed and expected values. These error terms were squared and summed, and the solver iteratively varied A and B to minimize the summed squared error terms. From the optimized values of A and B, the variation in flexural stiffness of the bone at any point along its free length could be estimated.

In vivo Patterns of Bone Strain

We selected *Pteropus poliocephalus* as our study species for all in vivo bone strain analyses because of their large body size (600–1,000 g for adults) and relatively robust wing bones, large enough for surgical attachment of small rosette and single element strain gauges [Swartz, 1991; Biewener, 1992]. All subjects were wild caught, from several locations around the University of Queensland, Brisbane, Australia, and then trained to fly the length of an outdoor flight cage (30 × 2 × 2 m) without stopping. Small rosette strain gauges (Tokyo Sokki Kenkyujo Co., Tokyo, Japan) were attached with a self-catalyzing cyanoacrylate adhesive to the dorsal, ventral and dorsolateral or medial midshaft cortices of the right humerus and left radius, as near as possible to midshaft but in areas free of direct muscle attachment to minimize localized distortions in overall bone strain due to muscle pull [Swartz, 1991; Biewener, 1992]. MCs and proximal phalanges III and V were instrumented in separate experiments with single element gauges on the dorsal and ventral or medial and lateral surfaces of the bone shaft. In all experiments, gauge wires were passed subcutaneously in a proximal direction from the gauge attachment sites on the digits, forearm or arm, then ventrally in front of the shoulder, and externalized through the skin of the thorax superficial to the sternum. Lead wires were then soldered to the connector with sufficient slack to permit large-amplitude wing movements without pulling gauges off the bones. Following postoperative recovery, 6–10 channels of strain data were amplified (Micromeasurements Model 2120AK strain gauge conditioner/amplifiers) and sampled at 250–400 Hz via a light-weight cable as each bat flew the length of the flight cage. Conventional videography (60 Hz) accompanied each recording.

Results

Limb Bone Allometry

Comparison of Regression Models

In phylogenetically based regression analyses, it is possible to distinguish three broad groups of traits: two kinds of groups in which a significant phylogenetic signal is present (those for which OU REG or Pagel GLS regression is preferred) and 1 group where little or no phylogenetic signal is discerned, in which OLS regression is preferred. Here, although both the OLS/GLS- and the RMA-derived regressions are presented, our description and discussion will focus on RMA slopes, derived from either OLS or regressions with phylogenetic information incorporated.

In our allometric analyses, the preferred model varied depending on the trait, with OU REG and OLS models preferred most often (table 2). Overall, characteristics of MCs and phalanges III and V exhibit the least phylogenetic signal. In two cases, the scaling of the lengths of the distal phalanges of the third and fifth digits, the regression model scaled with arbitrary branch lengths was preferred. In six cases, the scaling of the diameters of MCV and the diameters of the phalanges of both digits III and V, the model with even less phylogenetic signal, the OLS regression, was preferred. Hence, there is little phylogenetic signal in the scaling of lengths of the fifth proximal or third middle phalanges, or in the diameters of the MCs and phalanges overall. Comparisons of slope and intercept values in the OU or Pagel GLS regressions to previously published analysis of the same data that did not account for phylogenetic pattern show mixed results, with some slope and intercept estimates quite similar regardless of method, and others, particularly those with relatively lower sample sizes, differing substantially depending on method (table 2).

Scaling of Bone Lengths

Scaling of the lengths of most bones of the forelimb and hindlimb relative to body mass does not differ significantly between bats and nonvolant mammals (table 2; fig. 3). In only 2 measurements, MCIII and MCV, did the slopes of bone length versus body mass differ between bats and nonvolant mammals. In these cases, the bones of bats scaled

Table 2. Summary of allometric scaling of lengths and diameters of wing bones of bats

	Model	n	r^2	Nonvolant mammals			Bats			Nonvolant mammal versus bats			
				slope	RMA	intercept	slope	RMA	intercept	t_{slope}	p_{slope}	$t_{intercept}$	$p_{intercept}$
Humerus length	OU REG	259	0.83	0.348	0.382	1.724	0.297	0.325	1.967	2.433	*0.016*	5.286	
Radius length	OU REG	250	0.79	0.327	0.367	1.701	0.303	0.341	2.201	1.039	0.300	8.740	**0.000**
MCIII length	OU REG	183	0.89	0.401	0.425	1.206	0.241	0.256	2.013	6.231	**0.000**	19.982	
MCV length	OU REG	159	0.82	0.379	0.419	1.190	0.253	0.280	2.034	4.611	**0.000**	20.540	
PPIII length	OU REG	55	0.66	0.252	0.309	1.301	0.375	0.461	1.857	1.939	0.058	5.143	**0.000**
PPV length	OLS	57	0.82	0.291	0.322	1.161	0.336	0.372	1.650	0.946	0.348	6.524	**0.000**
MPIII length	OLS	27	0.83	0.289	0.316	1.064	0.358	0.392	1.906	0.496	0.625	3.531	**0.002**
DPIII length	Pagel GLS	34	0.73	0.287	0.336	0.702	0.309	0.362	1.762	0.319	0.752	4.884	**0.000**
DPV length	Pagel GLS	30	0.76	0.221	0.253	0.825	0.285	0.327	1.504	0.939	0.356	3.437	**0.002**
Femur length	OU REG	208	0.80	0.338	0.377	1.789	0.279	0.312	1.770	2.386	*0.018*	0.357	
Tibia length	OU REG	199	0.80	0.299	0.334	1.831	0.282	0.315	1.764	0.647	0.518	1.425	0.156
Humerus DV diameter	OU REG	239	0.93	0.371	0.385	0.668	0.337	0.350	0.756	1.828	0.069	2.839	**0.005**
Humerus ML diameter	OU REG	216	0.92	0.358	0.374	0.649	0.320	0.334	0.746	2.015	*0.045*	3.429	
Radius DV diameter	OU REG	225	0.90	0.348	0.367	0.484	0.324	0.341	0.668	1.199	0.232	5.453	**0.000**
Radius ML diameter	OU REG	213	0.86	0.364	0.393	0.474	0.318	0.343	0.706	2.162	*0.032*	6.809	
MCIII DV diameter	OU REG	158	0.83	0.367	0.403	0.238	0.350	0.386	0.374	0.524	0.601	2.731	**0.007**
MCIII ML diameter	OU REG	159	0.84	0.343	0.374	0.259	0.347	0.379	0.263	0.122	0.903	0.070	0.944
MCV DV diameter	OLS	137	0.90	0.318	0.335	0.241	0.307	0.323	0.444	0.492	0.624	6.178	**0.000**
MCV ML diameter	OLS	159	0.92	0.348	0.363	0.239	0.349	0.364	0.377	0.039	0.969	4.226	**0.000**
PPIII ML diameter	OLS	54	0.95	0.412	0.422	0.321	0.355	0.363	0.281	1.241	0.220	0.565	0.575
PPV ML diameter	OLS	55	0.96	0.364	0.371	0.299	0.374	0.381	0.265	0.241	0.811	0.530	0.598
DPIII ML diameter	OLS	35	0.95	0.386	0.396	−0.005	0.176	0.181	−0.248	3.589	**0.001**	2.571	
DPV ML diameter	OLS	29	0.94	0.354	0.365	−0.032	0.390	0.401	0.089	0.303	0.764	0.594	0.558
Femur DV diameter	OU REG	186	0.96	0.348	0.357	0.704	0.343	0.351	0.564	0.285	0.776	4.638	**0.000**
Femur ML diameter	OU REG	162	0.89	0.398	0.421	0.706	0.355	0.376	0.622	1.588	0.114	1.844	0.067
Tibia DV diameter	OU REG	187	0.93	0.347	0.359	0.726	0.328	0.340	0.468	0.801	0.424	6.611	**0.000**
Tibia ML diameter	OU REG	161	0.91	0.329	0.344	0.597	0.332	0.348	0.468	0.119	0.905	3.246	**0.001**

Bones tested include humerus, radius, MCIII and MCV, proximal and distal phalanges of digits III and V, femur and tibia. The model that provides the best fit to the data (OLS vs. GLS with arbitrary branch lengths [Pagel, 1994] vs. GLS with Ornstein-Uhlenbeck transformation) is listed in the model column, along with sample size, squared correlation coefficient, original slopes, RMA slopes and intercepts in subsequent columns. p values (d.f. = n − 4) are shown for slope and intercept differences between nonvolant mammals and bats. p values in bold are significant after correction for multiple comparisons; those in italics are less than 0.05 but not significant after the pFDR procedure. No p values are shown for intercepts when slopes differ significantly. PP = Proximal phalanx; MP = middle phalanx; DP = distal phalanx; DV = dorsoventral; ML = mediolateral.

with negative allometry (slopes less than 0.33; length α to $M^{0.26}$ and $M^{0.28}$, respectively) and nonvolant mammals with positive allometry (α $M^{0.43}$ and α $M^{0.42}$). For two lengths (humerus, femur), bats and nonvolant mammals differed significantly at $p < 0.05$, but based on the pFDR correction, these differences were not considered significant.

For traits where slopes did not differ significantly (i.e. no significant interaction effect), we were able to test for differences in elevation of the regression lines. Bones in the forelimbs of bats are significantly longer than those in nonvolant mammals (table 2, fig. 3). Due to differing femoral scaling between bats and nonvolant mammals, we were only able to test for significant difference in tibia length. The tibiae of bats show a trend toward shorter length than a nonvolant mammal of identical mass, although this trend is not statistically significant for this sample.

Scaling of Bone Diameters

With the single exception of the mediolateral diameter of the third distal phalanx in bats, bone diameters scaled close to isometry or with positive allometry in both bats and nonvolant mammals (table 2, fig. 4). In all measurements for which the slopes did not differ between groups, intercepts were compared between bats and nonvolant mammals. Bats have consistently larger diameters of forelimb elements than do nonvolant mammals, and significantly narrower hindlimb elements.

Mechanical Properties of Bone Tissue

Ash Content

The mineralization of the elements of the wing skeleton, as assessed by ash content, varies substantially by anatomical location and age (fig. 5–7). At birth, the ash content of all bones except the humerus and radius is less

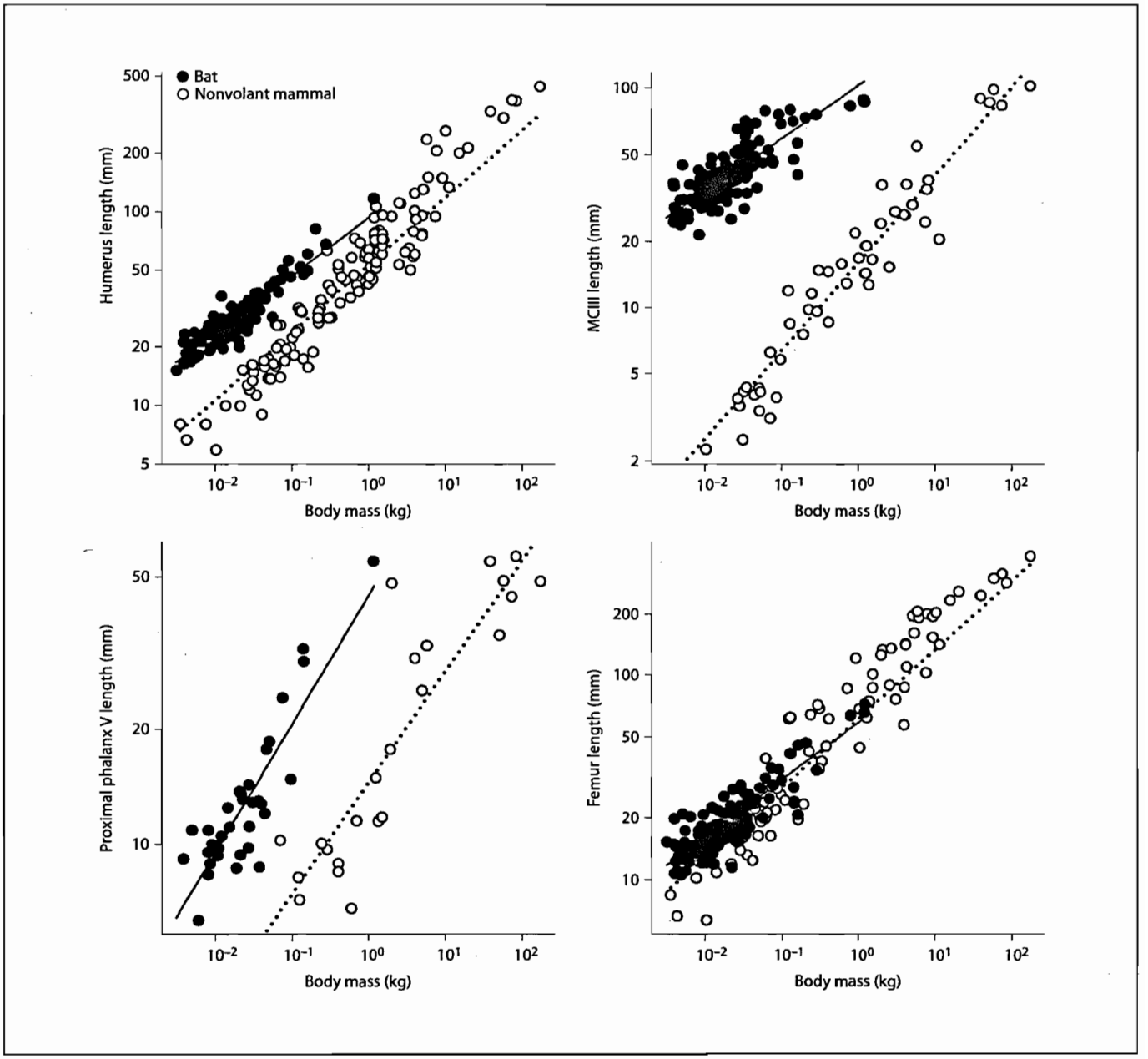

Fig. 3. Bone lengths versus body mass, log-log scale. Closed circles represent bats, and open circles are nonvolant mammals. Regression lines from the phylogenetic analyses are shown for each grouping.

than half of its mature value, and most bones reach adult mineralization levels only when the bat approaches adult body size. At all ages, mineralization varies in a proximodistal gradient, with ash content of the humerus greater than that of the radius, which is in turn more mineralized than the MCs, proximal, middle and distal phalanges in sequence. MCs vary in ash content as well, with mineralization of MCIII > MCV > MCIV > MCII during much of ontogeny, after which an increase in mineralization rate in MCV produces the adult pattern of mineralization: MCV > MCIII > MCIV > MCII. There is, however, considerable variation at each age, and sample size could influence these results. No mineral is detectable in the distal phalanges by ashing at any age.

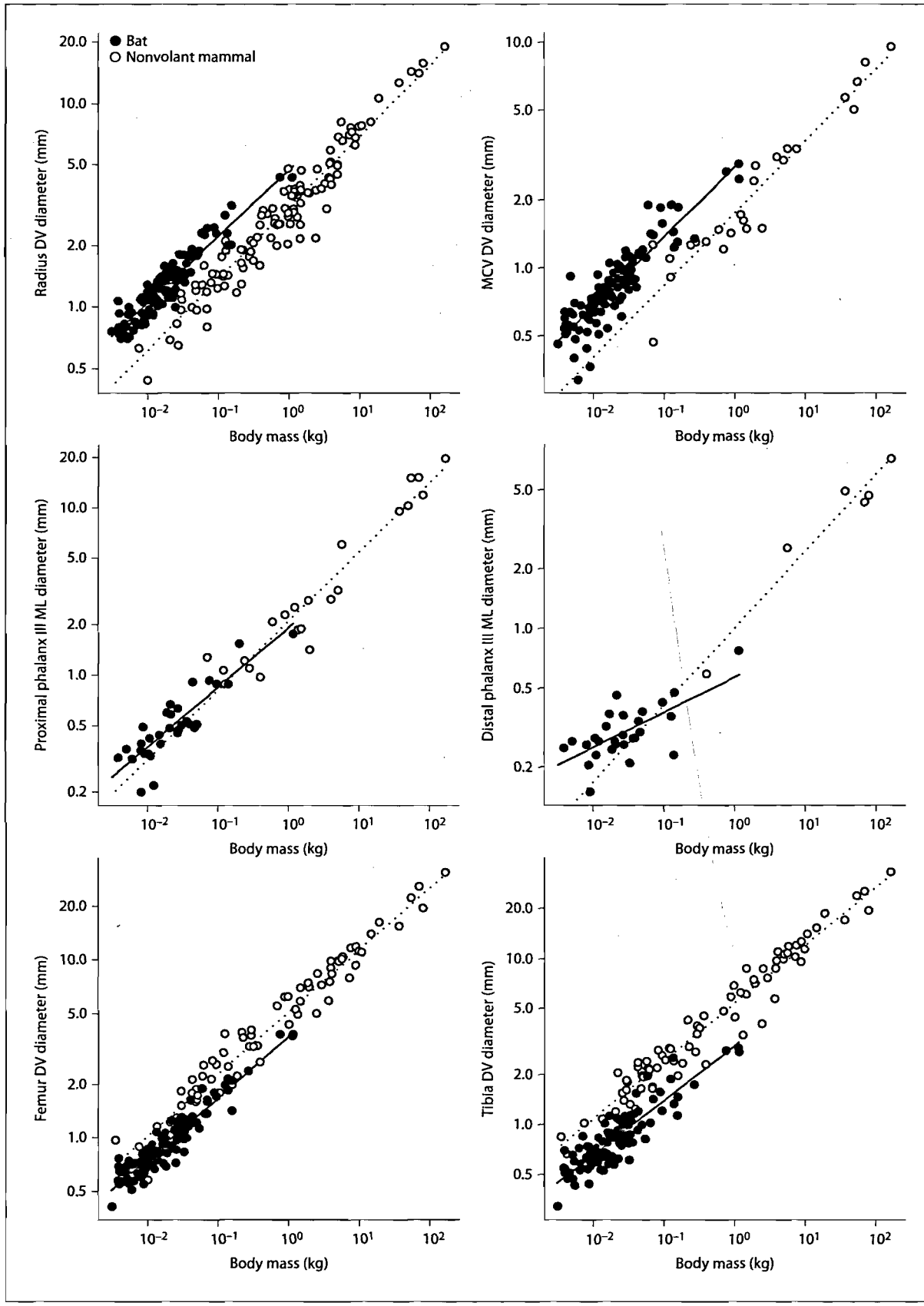
● Bat
○ Nonvolant mammal
Radius DV diameter (mm)
MCV DV diameter (mm)
Proximal phalanx III ML diameter (mm)
Distal phalanx III ML diameter (mm)
Femur DV diameter (mm)
Tibia DV diameter (mm)
Body mass (kg)
20.0
10.0
5.0
2.0
1.0
0.5
0.2
10^{-2}
10^{-1}
10^{0}
10^{1}
10^{2}

4

Mineralization increases with age in a nonlinear fashion for most bones, with the exception of the humerus and radius, in which the ontogenetic changes in ash content are nearly linear (fig. 6, 7). Typically, digits increase mineral content most rapidly early in ontogeny, followed by a period of less rapid mineralization and a final increase in mineralization rate near adulthood. No bones achieve adult mineralization levels until at or close to the age of onset of flight.

Histology

Microscopic examination of histological preparations shows fine-scale structure and mineral distribution in the middle and distal phalanx of digit I. Trichrome- and von-Kossa/safranin-stained sections demonstrate that the distal phalanx comprises a cartilage core, characterized by large, unmineralized, vacuolated cells, with little or none of the distinct collagenous extracellular matrix that would be observed in maturing, as yet unmineralized osteoid. This core is surrounded by a shell of collagenous tissue, typically less than 10 μm thick, with little or no detectable mineral deposition (fig. 8). There is no medullary cavity present, nor any sign of marrow tissue. In longitudinal sections, the entire proximal epiphysis of the distal phalanx is preserved, together with the distal interphalangeal joint and the distalmost portion of the third middle phalanx, comprising, along with nonmineral bone constituents, a bone of approximately cylindrical form with a slightly expanded distal epiphysis (fig. 8). Marrow spaces are visible among the bony trabeculae of the distal portion of the middle phalanx and the proximal portion of the distal phalanx, on both sides of the distal interphalangeal joint. Darkly staining hydroxyapatite is present in the distal part of the middle phalanx, capped by an articular surface of hyaline cartilage with a thickness of one cell layer. The proximal portion of the distal phalanx also possesses a single cell layer of articular cartilage overlying darkly stained, fully mineralized epiphyseal trabecular bone. This mineralized proximal layer is no more than 200 μm in length, and distal to the epiphyseal trabecular bone there is no further mineralization.

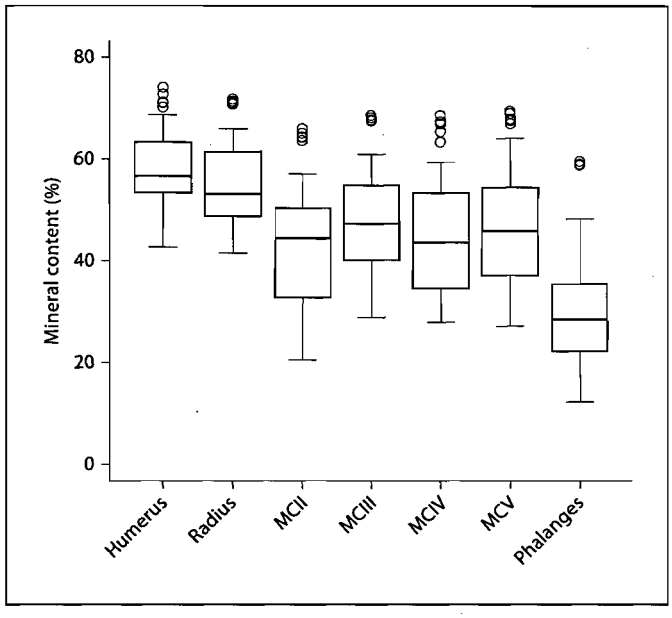

Fig. 5. Percent mineral content in 7 forelimb bones across ontogeny in *T. brasiliensis*. The box represents the interquartile range for nonadult observations, and the thick line represents the median. Adult mineralization values are represented by open circles.

Whole-Bone Bending

The magnitude of load needed to produce bone deflection equal to approximately 10% of bone length varied approximately 100-fold among the bones of the *G. soricina* wing (table 3). Force-displacement relationships were linear for all but one bone (MCIV), in which stiffness increased with increasing load (fig. 9). The flexural stiffness decreased in a proximodistal gradient along the wing as a whole and along the length of each wing bone (table 3). For dorsoventral bending, flexural stiffness at the proximal end of the bone ranged from a maximum of 156×10^{-5} N·m^2 for the humerus to a minimum of 1×10^{-5} N·m^2 for the middle phalanx of digit III.

For dorsoventral bending in digit III, mean Young's modulus *(E)* decreased proximodistally, ranging from 23 GPa for the proximal portion of the MC to 20 GPa for the most proximal part of the middle phalanx. Simultaneously, the second moment of area *(I)* decreased, ranging from 1.1×10^{-14} m^4 for the proximal portion of the MC to 3.7×10^{-16} m^4 of the proximal part of the middle phalanx. Consequently, the net flexural stiffness *EI* decreased from 20×10^{-5} N·m^2 for the proximal part of the MC to 0.99×10^{-5} N·m^2 for the proximal part of the middle phalanx.

Fig. 4. Bone diameters versus body mass, log-log scale. Closed circles represent bats, and open circles are nonvolant mammals. Regression lines from the phylogenetic analyses are shown for each grouping. DV = Dorsoventral; ML = mediolateral.

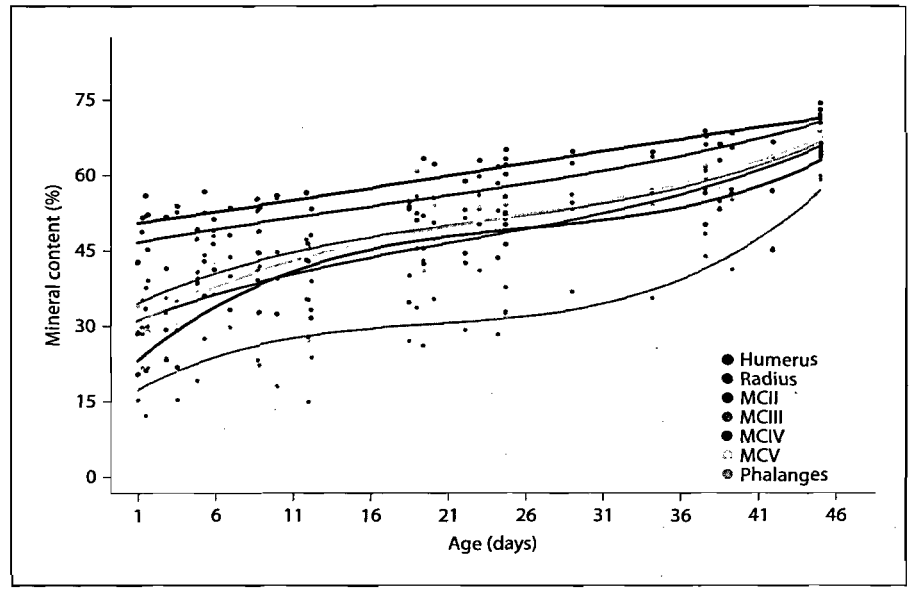

Fig. 6. Ontogenetic change in bone mineralization in the bat wing. Absolute percent mineral content across 45 days of ontogeny are shown with third-order polynomial fits. The humerus and radius consistently exhibit the highest mineralization, with phalanges the lowest.

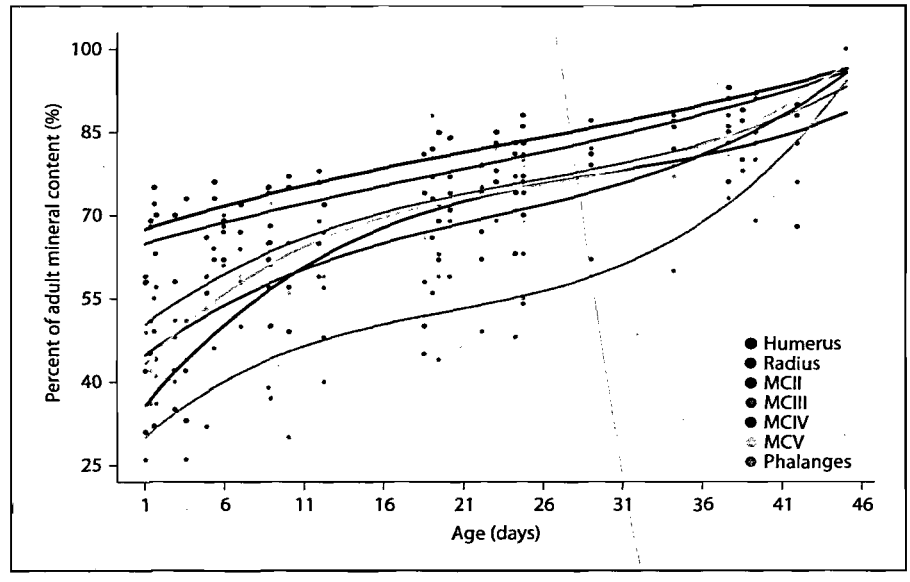

Fig. 7. Ontogenetic change in bone mineralization expressed as percentage of the adult mineralization value and third-order polynomial fit. Only the humerus and radius have more than 50% of adult mineralization at day 1, whereas the phalanges are mineralized at only approximately 30% of the adult value.

Bone Strain

For all sites from which we recorded bone surface strain, net loading changes dynamically throughout the wingbeat cycle with more than one and, in some cases, three or four strain peaks per wingbeat cycle (fig. 10, table 4). For some recording sites, these peaks occur in synchrony with the transitions between the down- and upstroke portions of the wingbeat cycle, but there are also numerous strain peaks without readily apparent gross kinematic correlates. Peak strain magnitudes for the humerus and radius are between ±1,500 and 2,200 με. For the third MC and proximal phalanx, peak strains on the dorsal and ventral bone surfaces are substantially greater, with the largest peaks near –3,000 and +6,000 με. On the medial and lateral surfaces of these bones, strain magnitudes are very low, typically less than 300 με. Orientations of peak strains deviate considerably from the bones' long axes for the humerus and radius. For the metacarpals and phalanges, large longitudinal strains of opposite sign on the dorsal and ventral bone surfaces, coupled with very low strains on the medial and lateral bone surfaces, suggest that these bones are loaded primarily in bending with respect to the plane of the wing.

Discussion

The Skeleton of the Bat Limbs in Comparison to Other Mammals: Allometric Perspective

The demands of powered flight clearly generate the primary selective regime under which the bat wing skeleton has evolved. Despite this unambiguous specialization for supporting a wing membrane in active flight, the skeleton of the bat limbs possesses many characteristics also observed in other mammalian groups, including extant primates and insectivores as well as extinct groups believed to represent the primitive condition for mammalian limbs. Bats retain all five of the primitive mammalian digits in the hands and feet, despite significant reduction of the pollex. Many of the other forelimb bones are elongated to varying degrees, depending on where in the wing they are found, with much greater elongation observed in the digital elements, the MCs and phalanges (table 2, fig. 3, 4) [Vaughan, 1959, 1970b; Swartz, 1997]. The more proximal forelimb elements, especially the humerus and radius, differ little in length or diameter from those of other mammals of similar body size [Vaughan, 1970b; Swartz, 1997]. The ulna is significantly reduced, retaining only the proximal articulation with the humerus and radius and a shaft of variable extent, from approximately 25–75% of the length of the radius, depending on species. The ulna retains no functional articulation with the carpus, although the carpus is relatively little changed from that of primitive mammals. The clavicle is retained in a form that resembles that of primates, dermopterans, tubulidentates, most insectivores and marsupials, and some lagomorphs, edentates and rodents [Eaton, 1944; Jenkins, 1974].

Despite extreme elongation of the manual digits, however, bats have retained many of the primitive functions of the mammalian hand. For example, many frugivorous bats use the digits to manipulate their food, with the thumb in particular playing a significant role in pteropodids [Vandoros and Dumont, 2004]. Bats have been observed employing their wings for numerous other nonflight activities, such as swimming, male-male aggression and assistance in delivery of pups [T.H. Kunz, pers. commun.].

Allometric Variation within the Bat Wing

All long bones of the bat wing are lengthened relative to their homologs in nonvolant mammals, but the degree of elongation varies substantially among elements (table 2, fig. 3) [Vaughan, 1970b; Adams, 1992a, 1998; Swartz, 1997]. The humerus and radius, although long in relation to body mass compared to many mammals in our sample, are no more elongated than those of specialized brachiating and knuckle-walking primates. It is only the bones of the digits that have undergone spectacular elongation in the evolution of the bat wing (fig. 3) [Vaughan, 1970b; Norberg, 1981; Swartz, 1997]. However, the pattern of bone dimensions in relation to body size in bats is unique when we consider the diameter of the bone shaft in addition to length alone. Scaling coefficients for bone diameters fall into two proximodistal classes, as for bone lengths, but with a notable difference. Dorsoventral

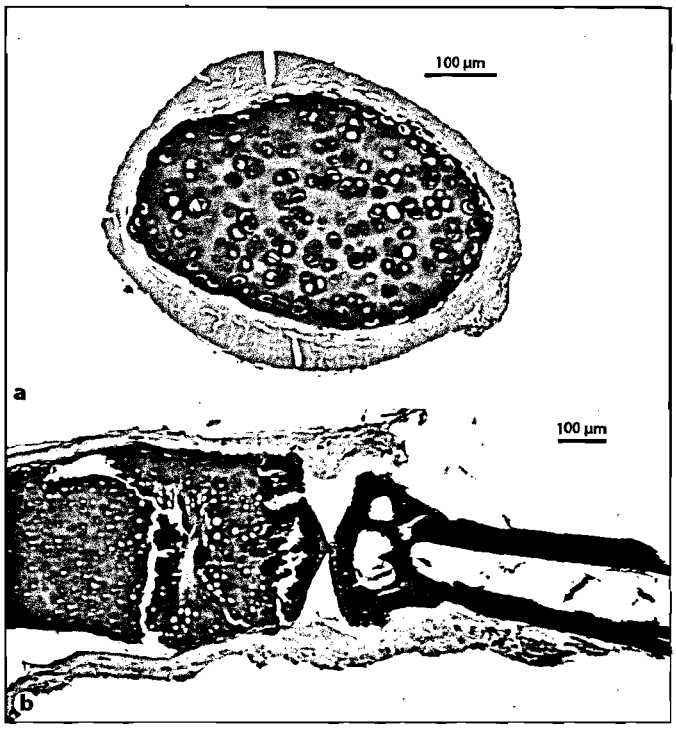

Fig. 8. a Representative cross-sectional view of an undemineralized third distal phalanx of an adult *T. brasiliensis* (von Kossa/safranin stained). Aqua blue staining in the outermost cortex of the bone depicts a thin shell of unmineralized collagenous tissue. The remainder of the tissue, darkly stained, appears to be largely cartilaginous, characterized by large, unmineralized, vacuolated cells, stained red, and lacking a true medullary cavity. **b** Longitudinal section of an undemineralized third distal phalanx, along with the third distal interphalangeal joint and the distalmost portion of the middle phalanx of a *T. brasiliensis* (von Kossa/safranin stained). The dark staining indicates deposition of calcium phosphate, most likely in the form of hydroxyapatite. Mineral can be seen in the distalmost portion of the middle phalanx, but extends only a short distance into the proximalmost portion of the distal phalanx, attenuating just distal to the level of the distal interphalangeal joint. The articular surfaces of both bones are capped with unmineralized hyaline cartilage.

Table 3. Summary of *EI* in the wing bones of one individual of *G. soricina*

	Length cm	Load at 10% × L deflection, N	*EI* proximal $(N \times m^2) \times 10^{-3}$	*EI* distal $(N \times m^2) \times 10^{-3}$
Humerus	1.50	1.034	1.56	0.50
Radius	2.91	0.337	1.31	0.47
MCIII	2.88	0.081	0.23	0.22
MCIV	2.81	0.056	0.98	0.18
MCV	2.02	0.053	0.12	0.03
Digit III phalanx I	0.90	0.132	0.04	0.02
Digit III phalanx II	1.19	0.019	0.01	0.003

EI was estimated using the Bernoulli-Euler bending equation for *EI* linearly changing along the length of the bone.

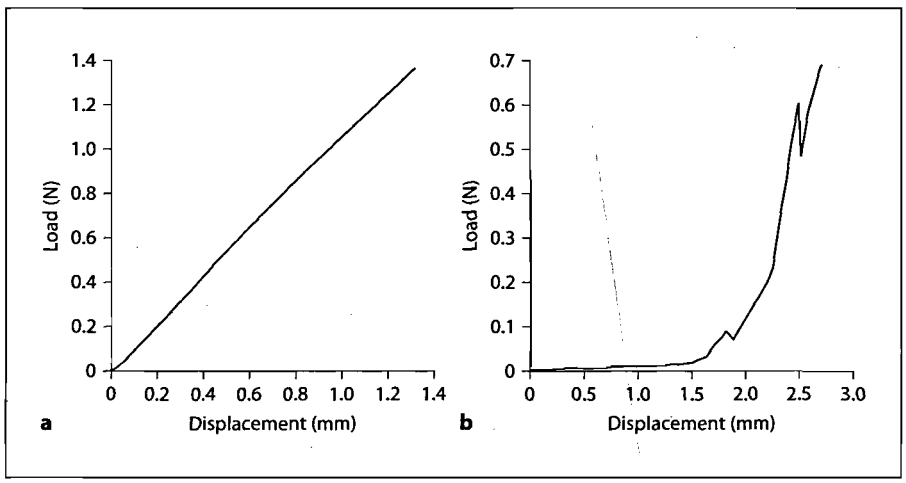

Fig. 9. Representative load-displacement curves for mechanical tests of bones from *G. soricina* wing. Load and displacement are related in a nearly linear fashion in the stiff humerus (**a**), but the more compliant distal elements (**b**, MCIV) show more complex behavior.

bone diameters, those perpendicular to the plane of the wing, are substantially greater than those of other mammals in the humerus, radius *and* MCs, although this pattern does not extend to the mediolateral diameters, those in the plane of the wing, except for the case of the fifth MC (table 2, fig. 4).

These differences between scaling of bone lengths and diameters must, ultimately, arise through differences in the ontogenetic development of different elements of the bat wing. Although aspects of the ontogeny of bat wing bones have been described [Adams, 1992a, b, 1998], new approaches in evolutionary developmental biology hold particular promise in this regard. Using *Carollia perspicillata* as a model system, recent work has identified differences in expression of bone morphogenetic protein 2, BMP2, as a critical factor underlying differences in the linear growth of MCs between bats and mice [Sears et al., 2006; this volume]. Upregulation of BMP2 causes cells in the hypertrophic cartilage zone of the MC growth plates of bat digits III, IV and V to proliferate and differentiate at high rates relative to the mouse condition; this results in a greatly enlarged hypertrophic zone [Sears et al., 2006; Sears, this volume]. BMP2, however, is found in only moderate amounts in the perichondrium of developing mammalian digits [Solloway et al., 1998], the region of the developing bone that will determine bone diameter through appositional growth. Cartilaginous condensations of the MCs in early embryos are similar in size in bats and mice, and it has been suggested that this may represent a key developmental constraint: the developmental program controlling the segmentation of skeletal primordial may be set up to create elements of similar size, predisposing adaptive changes in bone length to occur later in skeletal development [Sears et al., 2006; Sears,

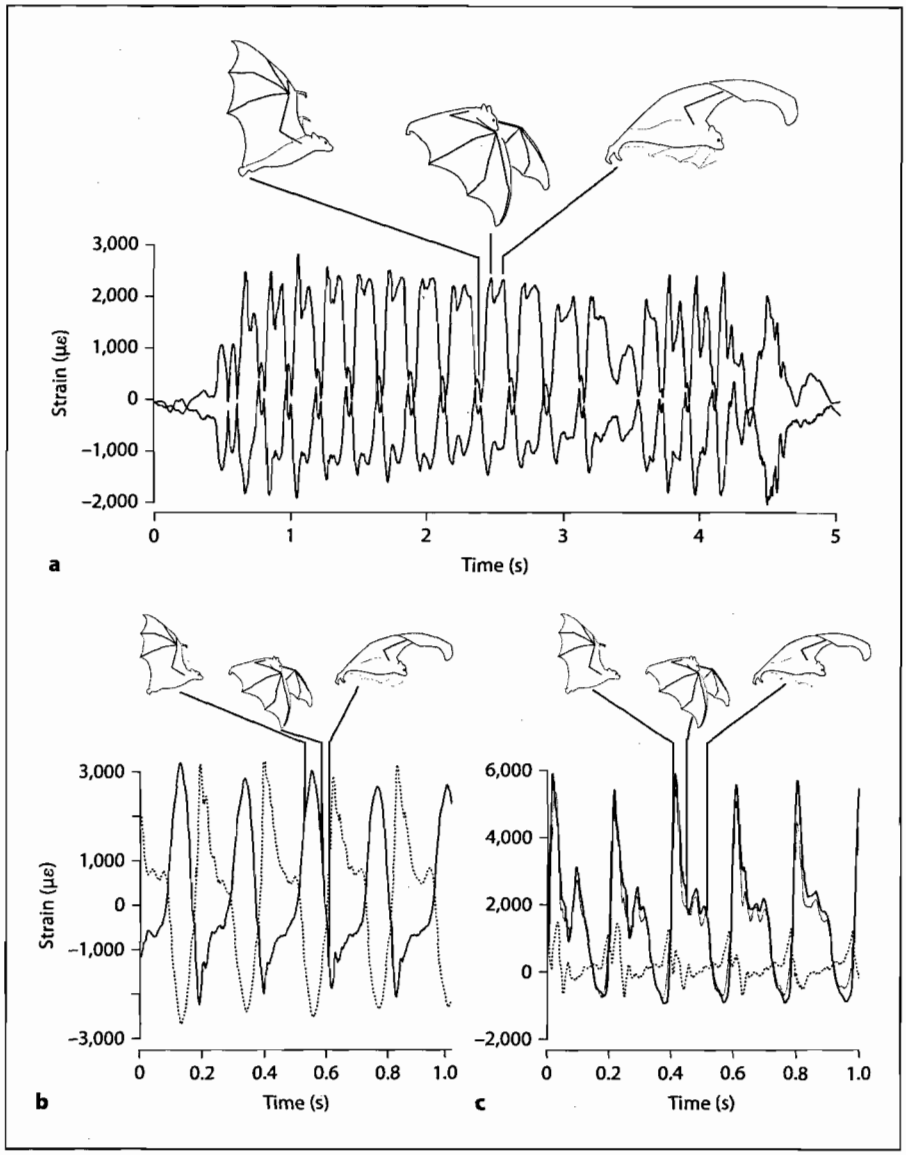

Fig. 10. Representative maximum and minimum principal strain records from the medial humerus (**a**), MCIII (**b**) and proximal phalanx III (**c**), correlated with flight kinematics based on videotapes (60 frames/s) taken during recordings. Strain magnitudes are reported in microstrain (change in length/original length × 10^{-6}); tensile (elongating) strains are positive, and compressive (shortening) strains are negative. The top panel depicts a complete flight sequence, from takeoff (small peaks at the far left), through a number of regular wingbeat cycles, through a postural shift in preparation for landing followed by five decelerating wingbeats and landing. The bottom panels show a smaller subset of wingbeats at a more expanded scale, with dorsal gauge locations depicted with solid and ventral with dotted lines. In all strain recordings, magnitude changes continually throughout the locomotor cycle for each recording site; representative top of upstroke, late downstroke, late upstroke and phases of one wingbeat are indicated by the schematics. Bone strains typically reach their greatest absolute values at mid downstroke and return to smaller peak values at the bottom of the downstroke and again at the top of the upstroke. Strain values return close to zero during some phases of the locomotor cycle.

this volume]. A relatively simple change in the level, but not in the temporal or spatial regulation, of BMP2 expression is thus able to produce the dramatically different morphologies of the bat and the mouse metacarpus. Further studies that probe patterns of BMP2 expression in elements proximal and distal to the MCs could help improve our understanding of the developmental origins of the scaling patterns recorded here.

Allometric Patterning in the Bat Hindlimb

Much discussion of bat skeletal structure has emphasized the considerable reduction of the hindlimb, seemingly in keeping with its greatly reduced role in locomotion [Vaughan, 1970a, b; Norberg, 1990]. However, although the hindlimb skeleton is reduced relative to the forelimb and to the hindlimb of mammals of comparable size, there has been little or no loss of the basal complement of bone elements. In this context, the three distinctive genera of blood-feeding Desmodontinae *(Desmodus, Diaemus* and *Diphylla)*, along with a few other taxa known to possess some specialization for terrestrial travel, such as *Mystacina tuberculata* and *Cheiromeles torquatus*, would appear to be the exceptions that prove the rule: having secondarily adapted a form of terrestrial quadrupedalism into their locomotor repertoire [Howell and Pylka, 1977; Altenbach, 1979; Schutt et al., 1997;

Table 4. Mean maximum bone surface strain values (με) measured during slow flight in *P. poliocephalus*

	Dorsal		Ventral		Medial		Lateral	
	magnitude	orientation	magnitude	orientation	magnitude	orientation	magnitude	orientation
Humerus								
Top of downstroke	488 (48)	0° (8°)	572 (46)	2° (4°)	468 (67)	25° (2°)	–	–
Mid downstroke	1,554 (162)	31° (3°)	1,496 (107)	22° (3°)	2,004 (120)	21° (3°)		
Bottom of downstroke	1,188 (81)	31° (4°)	988 (78)	21° (7°)	1,852 (105)	22° (2°)		
Radius								
Top of downstroke	−405 (99)	29° (7°)	−1,275 (96)	−10° (6°)	–	–	−2,184 (129)	21° (5°)
Mid downstroke	−1,808 (328)	28° (2°)	−1,316 (52)	32° (3°)			−2,012 (138)	32° (3°)
Bottom of downstroke	2,109 (263)	27° (3°)	243 (76)	29° (2°)			904 (83)	32° (4°)
	Dorsal		Ventral		Medial		Lateral	
	proximal	distal	proximal	distal	proximal	distal	proximal	distal
MCIII								
Top of downstroke	–	−1,488 (485)	580 (91)	2,115 (67)	81 (45)	–	96 (29)	–
Mid downstroke		−514 (89)	102 (43)	401 (23)	23 (32)		−121 (67)	
Bottom of downstroke		2,493 (234)	−1,213 (29)	−2,365 (43)	52 (82)		176 (40)	
Proximal phalanx III								
Top of downstroke	−592 (30)	−3,251 (607)	4,539 (196)	5,896 (407)	−152 (22)	–	303 (45)	–
Mid downstroke	−132 (3)	−480 (34)	2,140 (205)	2,346 (158)	−221 (10)		512 (80)	
Bottom of downstroke	126 (24)	1,430 (90)	−201 (39)	−433 (67)	893 (85)		−386 (48)	

Results are means and standard deviations (in parentheses) computed from measurements from between two and six animals and 50 and 248 individual wingbeats. Phase of the wingbeat cycle is determined by vertical motion of the wingtip. Tensile strains are positive and compressive strains negative by convention. The peak principal strain of greatest absolute value, negative for compression and positive for tension, is given for the humerus and radius, the bones large enough to instrument with rosette strain gauges, along with the orientation of the maximum principal strain to the bones' long axes [Swartz et al., 1992]. For MCIII and proximal phalanx III, only single-element gauges could be attached to the bone surfaces; values reported here are for gauges oriented longitudinally, along the bones' long axes.

Swartz, 1997; Schutt and Simmons, 2001; Riskin et al., 2005, 2006], they possess distinctly robust hindlimb long bones [Howell and Pylka, 1977; Swartz, 1997; Riskin et al., 2005] along with, in some cases, other unusual traits, such as a long digital flexor tendon locking mechanism for the pedal digits [Schutt, 1993; Simmons and Quinn, 1994]. However, the degree to which the hindlimb is truly reduced, and not simply dwarfed by the greatly elongated forelimb bones, is open to question [Swartz, 1997; Riskin et al., 2005]. Our allometric analysis, which includes relevant comparisons to nonvolant mammals, including most of the diversity of extant specialized gliders, points to the benefits of distinguishing variation in scaling patterns among bones. Tibial diameters, but not length, are substantially more reduced relative to nonvolant mammals than those of the femur. Indeed, femur length relative to body mass is largely overlapping in bats and nonvolant mammals (table 2, fig. 3).

Flight itself may dictate some of the selective benefits of retaining relatively robust hindlimb skeletons, even at the cost of additional mass that not only requires nutritional resources to grow and maintain, but also to be carried in every flight. Because of the direct incorporation of the hindlimb into the wing in bats, in direct contrast to the condition in birds and insects, hindlimb length is a major determinant of both the wing chord and surface area of the plagiopatagium. As an integral element of wing structure, the hindlimb may possess functionality beyond passive anchoring of the wing membrane. Detailed three-dimensional analysis of wind tunnel flights of *Cynopterus brachyotis* demonstrates that hindlimb excursion during the wingbeat cycle is substantial and three-dimensionally complex [Tian et al., 2006]. Moreover, the timing of the motions of the hindlimb relative to those of the forelimb skeleton and body is staggered, out of synchrony with the wing. This suggests that it is likely that active movements at the hip and/or knee and/or ankle contribute significantly to flight performance, perhaps by playing an active role in modulating the tension in the wing membrane, particularly the plagiopatagium. This hypothesis, however, requires direct testing using electromyographic recording of activity in the

hindlimb musculature during flight. Without such direct testing, it is impossible to determine whether the muscles of the pelvis and hindlimb or those of the carpus and fifth digit, perhaps plus the intrinsic musculature of the wing membrane, drive the motions of the hindlimb during flight. If further kinematic and electromyographic study supports the idea that the hindlimb is instrumental to the mechanics of the bat skin membrane, we propose that gaining better insight into the role of the hindlimb in the mechanics and aerodynamics of bat flight may also lead to improved understanding of the flight of extinct pterosaurs. After a long period of debate concerning the role of the hindlimb in pterosaur wing structure, it now appears that evidence strongly supports the inclusion of much or all of the hindlimb in the wing membrane [Unwin and Bakhurina, 1994; Unwin, 1999]. Models of pterosaur aerodynamics [Wilkinson et al., 2006; Wilkinson, 2007] could be readily modified to account for potential effects of active hindlimb positioning and membrane stiffness modulation.

Phylogenetic Patterns

We report here the first analysis of limb bone allometry in bats that is carefully controlled for phylogenetic relatedness. This more rigorous approach demonstrates that scaling relationships reported earlier [Swartz, 1997] prove to be relatively robust to assumptions regarding phylogeny. Phylogenetically scaled branch lengths best fit the distribution of data for only two of the variables tested: the lengths of the distal phalanges of digits III and V (table 2, fig. 4). This result demonstrates that distal phalanx length within bats is determined not only by body mass, but also varies among taxa, independently of body-size-associated variation.

This result is striking in light of the results of bone ash content and histological study of the wing bones of *T. brasiliensis* (see also below). Ashing revealed only a small amount of bone mineral in the *T. brasiliensis* phalanges, and no measurable mineral in the distal phalanges (fig. 5). Histological preparation with calcium-sensitive staining demonstrated a small calcified region in these bones, limited to the proximal portion of the distal phalanx, immediately underlying the articular cartilage of the distal interphalangeal joint (fig. 8). This result suggests that the developmental program for the formation of early bone precursors, their subsequent growth, and progressive mineralization has been modified to an extremely high degree in the bat distal phalanx, at least in this species. Unfortunately, we do not have this degree of detail concerning structure of the distal phalanx for other species at present, but we hypothesize that it is likely that the distal phalanges are relatively poorly mineralized in most, if not all, bats.

Our mechanical tests of *G. soricina* wing bones demonstrate physical behavior that is consistent with this hypothesis. The middle phalanx of digit 3 shows by far the steepest gradient in flexural stiffness, *EI*, within any single bone in the *G. soricina* wing (table 4). Moreover, the largest proximodistal decrease in flexural stiffness occurs at the proximal interphalangeal joint, between the proximal and middle phalanges, with the distal value of *EI* of the middle phalanx nearly an order of magnitude lower than that of the proximal phalanx (table 3). The distal phalanx in this bat was too small for study using this method, but would likely have been characterized by a similar or even more extreme pattern. A more detailed study of the dimensions and material properties of manual phalanges is clearly warranted.

Functional Consequences of Compliant Distal Wing Bones

At present, our understanding of the mechanical, aerodynamic and energetic consequences of highly deformable distal wing bones is limited. One possibility is that the low stiffness of these bones facilitates passive structural alignment of the wing with dynamically changing airflow patterns. The outermost parts of flapping wings, be they in bats, birds, insects or human engineered devices, intrinsically travel at higher speeds and experience higher angles of attack with respect to the flow, simply due to the geometry of flapping. Flow separation, and its associated increases in turbulence and drag and concomitant decreases in ease of flight path control, is much likelier if the wing tip is stiff. Flexible distal bones can allow passive wing rotation, deformation and decambering, which may delay or avoid flow separation. In addition, the metabolic cost of accelerating and decelerating limbs can be a substantial portion of locomotor energetics. The low mineralization and hence greatly reduced density of the distalmost parts of the skeleton can make a significant contribution to mass reduction at the very part of the wing where the metabolic penalty is greatest, i.e. far from the wing's center of rotation, which is near the shoulder joint, or perhaps the sternoclavicular joint [Swartz et al., 2005]. Finally, the wing tip is highly vulnerable to damage both during flight, and, in particular, during landings, male-male aggression and diverse additional behaviors. Low mineralization and the associated low values of bone tissue stiffness and strength are associated with greatly improved work to fracture

[Currey, 1984, 2002], hence the bone of the wing tips may be far more resistant to breakage than stiffer bones would be.

Comparisons to Gliders

Much work on the origins of flight in bats has adopted the view that bat wings derive from precursors similar to the patagia of extant mammalian gliders. In particular, traditional views linking bats to dermopterans, primates and tree shrews as an archontan clade posit evolutionary continuity between the limb structure of Dermoptera and Chiroptera. However, modern phylogenetic perspectives, based on both molecular and morphological evidence, provide little or no support for a special relationship between bats and any of the seven lineages of mammalian gliders [Springer et al., 2001, 2004; Teeling et al., 2002, 2005]. Moreover, the morphology of extant gliders appears to have evolved independently numerous times, with the many distinct lineages of gliding mammals converging on quite similar body plans, down to a relatively fine level of detail. A striking example of this parallel evolution is the distinctive pattern of innervation of the muscle in the leading edge of the patagium in both bats and dermopterans (the occipitopollicalis complex and propatagialis, respectively) [Thewissen and Babcock, 1991]. In both orders, this muscle receives a highly unusual dual innervation in which the proximal region of the muscle is innervated by the facial nerve, cranial nerve VII, and the distal portion of the muscle by cervical spinal nerves. Thewissen and Babcock [1991] considered parallel evolution of this innervation pattern so unlikely that they proposed that its presence in both bat and dermopteran clades constitutes a nearly irrefutable synapomorphy, both for a monophyletic bat clade and a monophyletic lineage of bats plus dermopterans. However, this supposedly unique innervation pattern has been documented in one of the rodent lineages of specialized gliders, the pteromyine flying squirrels [Chickering and Sokoloff, 1996], hence it must have arisen at least twice, in bats plus dermopterans and in sciurid rodents, and at least 3 times if bats and dermopterans are not sister taxa. To our knowledge, there are as yet no studies confirming the presence or absence of this innervation pattern in the other lineages of mammalian gliders.

Thus, the best available evidence indicates that the basic body and limb structure of mammalian gliders has arisen independently many times, given the current phylogenetic understanding that no glider lineage has any special relationship to bats, and no members of the Laurasiatheria, the clade containing bats, Carnivora, Eulipotyphlans, Perissodactyla, Cetartiodactyla and Pholidota, show any signs of gliding behavior or gliding specialization. However counterintuitive, this evidence suggests that the time may be ripe to develop and explore alternative hypotheses regarding the origin of bat flight that do not include a stage that closely resembles extant gliding mammals.

Mechanical Properties of Bat Wing Bones

The mechanical performance of skeletal structures depends on the complex interplay among load applied, bony geometry and tissue material properties. The variation in the mechanical characteristics of the compact bone material of vertebrate limbs is small relative to variation in gross bone geometry, and it is reasonable to assume constancy of bone mechanical properties, such as stiffness or strength, in comparative biomechanical analysis of mammalian limbs. It has been suggested that bone tissue comprising approximately 65–70% hydroxyapatite and 30–35% organic components, primarily collagen, represents an effective, if not optimal, compromise among the competing needs for maximizing strength and stiffness and minimizing weight [Currey, 1984, 2002, 2003].

The bony tissue of the bat wing skeleton, however, differs substantially from the otherwise conservative pattern observed in mammalian limb bones (table 3, fig. 5–8). In the proximal region of the wing, bone mineralization levels are comparable to those reported for other mammals, but there is a substantial decline in wing bone mineralization along the wing's proximodistal axis. Mean bone ash, a direct measure of the proportion of bone tissue composed of inorganic material, decreases from the humerus to the radius, from the radius to the bones of the digits, and from MCs to proximal to more distal phalanges within each digit. In those bones in which it has been possible to test mineralization at a finer spatial scale, mineralization levels also decrease distally (table 3). In the distal phalanges of at least some bat species, there may be little or no mineral impregnation of the collagenous osteoid except in the subchondral compact bone and the immediately underlying trabecular bone tissue, just deep to the articular cartilage of the proximal end of the distal phalanx (fig. 8).

We note, however, that some care should be given in the interpretation of the results of the cantilever bending experiments we present here. First, the Bernoulli-Euler bending equation is strictly accurate only for small deflections of an ideal beam. In our tests, deflections were often quite large, even at relatively low loads. And, bat bones differ from ideal beams in several ways; they are

not homogeneous in mechanical properties along the bone's length, they do not possess constant cross-sectional area or shape, and there may be variation in mechanical properties of bone tissue even within a cross-section, although this has yet to be demonstrated for bats as it has for some other species [Ziv et al., 1996; Rho et al., 2001]. However, although bat bones are certainly not ideal beams, we feel that this approach produces reasonable estimates as a first approximation, particularly when comparing values among bones within a single wing of a single bat. Second, we note that we modeled the proximodistal change in *EI* as a monotonically decreasing linear function because bat wing bones taper, decreasing in diameter and hence *I* distally [Swartz, 1997]. However, percent mineralization also decreases in a proximodistal gradient, hence both *I* and *E* change along the length of wing bones. As a consequence, a higher-order estimation of *EI* may be warranted. Our trials of parabolic or cubic estimates, however, performed poorly, and some more complex pattern of joint change in *E* and *I* may be the condition in bat wing bones. These limitations highlight the need for direct local measurements of Young's modulus, the second moment of inertia or, ideally, both, at a scale appropriate to documenting variation within each bone.

We propose that some of these challenges can be addressed by adoption of two specific techniques that can facilitate measuring bone geometry and material properties at the spatial resolution necessary to understand the mechanics of bat wing bones. In bones of the size of those of bat digits, it is critical to quantify cross-sectional shape precisely. Microscopy is often poorly suited to this task; although histological preparation followed by microscopic examination facilitates measurement at the appropriate scale, relatively small distortions can have a large impact on estimates of the second moment of area, *I*, which includes a term that raises distance of each areal increment to the fourth power. We suggest that micro-CT scanning, an increasingly accessible technique, is well suited to the precise and nondestructive measurement of cross-sectional geometry of small skeletal specimens [Feldkamp et al., 1989; Ruegsegger et al., 1996; Barbier et al., 1999; Borah et al., 2000; Laib et al., 2000; Mulder et al., 2004].

We also propose that nanoindentation [Turner et al., 1999; Van Landingham, 2003; Radovic et al., 2004; Chen et al., 2006; Kim et al., 2006; Ma et al., 2006; Orso et al., 2006] is a promising technique for ascertaining mechanical properties of bone samples too small to test by conventional material testing, and for resolving variation in mechanical properties on a microscopic scale. This approach employs a microscopic indenter, typically 1–10 μm in diameter, that can be applied to a prepared surface with a small, precisely measured force, in the range of tens to hundreds of millinewtons, to a controlled depth, typically hundreds to thousands of nanometers. The response of the calibrated system can then be used to accurately compute material stiffness, as well as other elastic constants, and, with the proper application, nanoindentation can also be used to assess fracture toughness as well [Li and Bhushan, 2002; Field et al., 2003; Scholz et al., 2004]. This approach is beginning to be applied in bone biology with great success [Erickson et al., 2002; Goodwin and Sharkey, 2002; Hengsberger et al., 2002; Wang et al., 2002] and is ideally suited to assessing mechanical properties of the small, delicate bones of bats. With more accurate assessments of bone stiffness and elastic behavior, combined with precise quantification of the structural geometry of bat bones, it will be possible to gain a far better understanding of the way bones of the bat wing respond to the forces imposed on them during flight and other behaviors.

In vivo Assessment of Bone Loading in the Wing Skeleton of Pteropus poliocephalus

The natural loads experienced by bones are complex; they vary in both magnitude and orientation during each locomotor cycle or event. These time-varying patterns, in turn, vary with speed, acceleration, asymmetry, etc. When this loading complexity is combined with the three-dimensionally intricate geometries of bones, it is difficult or impossible to accurately predict skeletal stresses a priori, at least not without sophisticated modeling approaches such as finite element analysis [for examples, see Combes and Daniel, 2003; Dumont et al., 2005; Dumont and Swartz, in press]. This general difficulty is exacerbated in bat flight for several reasons. Long slender bones, such as those of the bat wing, are very sensitive to bending loads, with small increments in bending forces leading to large strain changes. The aerodynamic forces of flight involve not only flapping but likely unsteady fluid dynamic effects, leading to enormously time-dependent and often unpredictable loads. Additionally, although students of terrestrial locomotion can empirically assess ground reaction forces with force plates, direct measurement of aerodynamic forces is far more challenging. At present, in vivo skeletal mechanics can be assessed only by measuring the patterns of deformation of the bones directly [Swartz, 1991; Biewener, 1992]. For bat biology, this approach is inherently limited to the larger

bones of the largest bats. Nonetheless, direct measurement of bone surface strain is a unique and valuable source of information. For a given real bone of three-dimensionally intricate shape, inhomogeneous mechanical properties and anisotropy, combined with a particular time-varying and poorly understood set of forces applied to the limb by a natural locomotor behavior, there will be a particular pattern resultant strain. Although knowing strain alone cannot unambiguously delineate the detail of the nature of the loading or mechanical characteristics of the bone, it will place stringent limits on possible combinations and suggest loading regimes that are relatively more and less likely to take place in nature.

In the work described here, originally presented in Swartz et al. [1992], we used in vivo analysis to directly determine the surface strains on the armwing bones of several *Pteropus poliocephalus* during level, steady flight at moderate speed. Strains recorded from each bone indicate complex loading regimes. Principal strain profiles for each humeral and radial recording site show a triphasic pattern, with peak loads occurring at the middle of the downstroke, the bottom of the downstroke and the top of the upstroke. Between these peaks, strain magnitudes drop considerably, approaching zero during the upstroke (fig. 10). Peak strain magnitudes (table 4) are similar to those recorded from terrestrial mammals during moderate locomotor activities [Biewener and Bertram, 1993; Yoshikawa et al., 1994; Mikić and Carter, 1995; Demes et al., 1998; Coleman et al., 2002]. Orientations of peak principle strains at these sites deviate significantly from zero, with overall mean orientations of 23° for the humerus and 30° for the radius (based on the mid downstroke and bottom of downstroke peaks). This pattern of off-axis strain of similar magnitude around the bone circumference demonstrates significant torsional loading.

Longitudinal stresses calculated from the raw strain data are comparable in magnitude to stresses developed in other mammals during fast canters, gallops and some jumps [Biewener et al., 1983; Swartz et al., 1992; Biewener, 1993; Biewener and Dial, 1995]. Transverse stresses are large, particularly at the bottom of the downstroke, and shear stresses are also significantly greater than in other mammals (greater than 15 MPa, in comparison with previously published values of no greater than 6 MPa, recorded during walking and running in humans and dogs [Carter, 1978; Carter et al., 1980]). These large transverse and shear stresses are both consistent with substantial torsional loads.

The direct measurements of MC and phalangeal strains reported here demonstrate a dramatically different pattern of loading in the MCs and proximal phalanges, the most distal bones of the handwing from which we have successfully recorded strains. Although the small diameter of these bones, even in the largest of bats, prohibits the use of rosette strain gauges, the total evidence of longitudinal and transverse strain gauges defines MC and phalangeal loading well, pending more detailed or sophisticated studies. In every case in which longitudinal and transverse single element strain gauges were implanted in tandem, only a few millimeters apart, longitudinal strains were far greater than those measured at 90° to the bones' long axes, by a factor of 3.1–3.4. For a solid object loaded along its long axis, strain at right angles to that axis, the transverse strain or $\varepsilon_{transverse}$, will be $-\nu\varepsilon_{longitudinal}$, where ν is Poisson's ratio and $\varepsilon_{longitudinal}$ is the strain along the long axis. Although we were not able to measure Poisson's ratio from the bone material of bat digits, the published value of Poisson's ratio for compact cortical bone of mammals of approximately 0.3 [Zysset et al., 1999; Dong and Guo, 2004] is well matched to the 3.1 to 3.4 to 1 ratio of longitudinal to transverse strain we observe here. If the MCs or phalanges experienced substantial torsional or shearing loads, or predominantly multiaxial loading, the ratio of transverse to longitudinal strain would not approach the Poisson's ratio for bone.

The dorsal versus ventral surfaces of the MCs and phalanges also exhibit strains that are opposite in sign but roughly similar in magnitude, and low, often approaching zero, on the medial and lateral (in the wing membrane plane) aspects of the bones. This pattern is consistent with bending of these bones about a transverse axis, perpendicular to the bones' longitudinal axes, in and out of the plane of the wing membrane. The peak strain values for these bones often vary between negative, or compressive, and positive, or tensile, strains, suggesting that the orientation of this bending goes through a reversal during the wingbeat cycle, with the bones bent in a dorsally concave sense during the downstroke and a ventrally concave sense during the upstroke. This is consistent with a net upward force on the wing during the downstroke, as we would expect from the aerodynamic forces. During the upstroke, it is likely that the inertial effects of the deceleration of the wings in the second half of the downstroke followed by acceleration in the opposite direction produce the reverse in orientation of bending.

We also observe a distinct gradient in strain magnitude along the wing's span. On both dorsal and ventral surfaces, strains increase in magnitude from MC to phalanx, and also along the length of both the MCs and pha-

langes (table 4, fig. 10). Because strain measurement provides only information about the net interaction of applied load, material properties, and the geometry of load application and the structure experiencing the load, it is impossible to determine from these data whether this gradient reflects a gradient in load, bone cross-sectional geometry, stiffness or some combination of these. However, the bones of large *Pteropus* do not deviate from the typical bat pattern of decreasing diameter from the humerus out to the distal phalanges, coupled with decreasing diameter, or taper, along the lengths of the MCs and phalanges (fig. 4) [Swartz, 1997]. This geometric pattern alone may account for increasing strain toward the distal wing extremity, and any trend toward decreasing mineral content or increasing load would only magnify this effect.

Thus, the armwing and handwing differ dramatically in both structure and mechanical performance. Bones of the armwing are relatively highly mineralized and rigid, only slightly elongated, of greater diameter than homologous bones of similarly sized mammals, possess thin walls and large medullary cavities, and are loaded in a complex fashion with torsion and shear dominating (fig. 3–5, 9; tables 2–4) [Swartz et al., 1992; Swartz, 1997]. Bones of the handwing, particularly the phalanges, are poorly mineralized and thus relatively compliant, tremendously elongated but without expanded diameters, thick-walled with little to no medullary cavities, and are loaded in bending, in a concave-upward fashion during the downstroke and in the opposite sense on the upstroke. Armwing torsional stresses likely arise from the lack of congruence between the wing's center of pressure and the anatomical position of the humerus and radius in the wing membrane, giving the net aerodynamic force a large torsional moment about the bones' long axes. Because the center of pressure of complex flapping wings likely moves during flight, we expect wing twisting to be a common feature of all flying animals, a prediction borne out by the available evidence from birds and insects [Wootton, 1993; Biewener and Dial, 1995; Ennos, 1995; Daniel and Combes, 2002; Combes and Daniel, 2003]. In bats, these torsional forces are accommodated effectively by the combination of bone geometry and mechanical properties. In contrast, little or no torsion is transmitted to the skeleton in the handwing, but bending arising from inertial and, likely, aerodynamic effects is large. With limited rigidity at the joints and within the bones themselves, very large strains result.

Regardless of the proximate cause of the bone strain gradient in the bat handwing, the effect on bone mechanics is extreme. We recorded peak strain magnitudes of over 2,400 and 6,400 $\mu\varepsilon$, respectively, in the MC and proximal phalanx of digit 3 (table 4, fig. 10) in these experiments, in which the bats flew at only moderate, steady speed, with no ascent or descent, and no turns or maneuvers. We would expect that more extreme locomotor behavior would induce even larger strain values, perhaps by as much as two- to fourfold. As far as we know, the strains we recorded from proximal phalanges of *P. poliocephalus* are the largest bone strains yet recorded in vivo, and we expect that strains in more distal elements during mechanically demanding locomotor behaviors could be as much as 10 times higher. This prediction is in keeping with our understanding of the mechanical properties of bone tissue in the distal wing elements: highly mineralized compact bone material would exceed its failure strain at these values, but because failure strain is inversely related to bone mineralization, the low mineral content of distal bat wing bones may be a necessity in structures experiencing this high degree of bending. This ought, perhaps, to have been something we predicted in advance of direct measurement; bat phalanges are not only quite poorly mineralized and therefore characterized by low elastic moduli, their relatively small external diameters and lack of medullary cavities result in very low values for second moment of area, both traits that will promote rather than limit bending. The substantial bending of greatly elongated elements, in turn, dictates one of the distinctive aspects of bat flight kinematics, the tendency for wing tip reversal to occur near the downstroke-to-upstroke transition [Rayner et al., 1986; Swartz et al., 2005; Norberg and Winter, 2006; D.K. Riskin, pers. commun.].

Future Directions

The four known evolutionary acquisitions of flight share characteristics dictated by physics but have been uniquely shaped by distinct phylogenetic histories and morphological 'starting points' that have resulted in important variation in wing structure and flight performance. Bat flight is presently the least well understood mode of flight of extant animals. For insects, understanding of flight has been revolutionized by contemporary fluid dynamic methods [Ellington et al., 1996; Birt et al., 1997; Van den Berg and Ellington, 1997b; Willmott et al., 1997; Dickinson et al., 1999; Dickinson, 2000; Tytell and Ellington, 2000; Birch and Dickinson, 2001; Sane and Dickinson, 2002]. Experimental studies of tethered and freely flying animals have been integrated with computational fluid dynamic and physical model-

ing of wake structure [Birch and Dickinson, 2001], and have revealed mechanisms responsible for the generation of aerodynamic forces. Recent studies of bird flight have similarly advanced the subject [Spedding et al., 2003; Dial, 2003; Hedrick, 2003; Hedrick et al., 2004; Usherwood et al., 2005]. But bat flight clearly differs from that of insects and birds in substantial ways. These include the proportions of the bones of the wings and hindlimbs, the mechanical properties of the bones of the wing, and the loads experienced by the bat skeleton during flight. In addition, however, there are other traits that relate directly to flight mechanics, including the possession of more than two dozen joints under partially independent control [Norberg, 1970, 1972; Vaughan, 1970a, b; Swartz, 1997], tremendously anisotropic wing membrane skin with both substantial variation and adjustable stiffness across the wing [Swartz et al., 1996; Swartz, 1998] and a distributed network of skin sensory organs believed to provide continuous information regarding flows over the wing surfaces [Zook and Fowler, 1986; Crowley and Hall, 1994; Zook, 2005, in press]. To understand how bats achieve their remarkable flight performance will require integration of these subjects into a more synthetic view.

Equally pressing is the need to tackle the aerodynamics of bat flight and to analyze skeletal, muscular and dermal specializations in the context of the relevant physics. Bat flight consistently employs negative and extreme positive angles of attack, large and dynamically changing camber and complex three-dimensional wing topology, even for 'simple' constant speed and level flight of bats [Swartz et al., 2003, 2005]. Clearly, there are fundamental differences between bats and the large, fast aircraft for which aerodynamic theory has been developed, yet there is as yet little understanding of the aerodynamic functions of the bat wing's dynamically changing form, or of the roles of morphological and physiological specializations in determining flight performance. At the Reynolds numbers at which bats fly ($10^3 < Re < 10^6$), the effects of viscosity are not negligible, as they are for even the smallest airplanes. In this *Re* range, flow over foils can be turbulent, unsteady and unpredictable, and basic parameters, such as wing aspect ratio, angle of attack, camber, etc., can influence flow patterns and aerodynamic forces in dramatically different ways than in higher *Re* flows [Smith and Shyy, 1996; Shyy et al., 1999a, b; Levin and Shyy, 2001; Lian et al., 2003]. Because wing structure and flight behavior differ fundamentally between bats and other flying animals, the mechanics and aerodynamics of bat flight cannot be extrapolated from studies on birds or insects, and experimental analysis, physical modeling and numerical simulation of bat flight will have distinctive characteristics. In particular, unsteady effects and interaction of the wings and/or body with wakes generated earlier in the wingbeat, as seen in even large and fast insects [Ellington, 1984; Van den Berg and Ellington, 1997a; Müller et al., 2000; Ramamurti and Sandberg, 2002], are probably crucial to bat flight physics, especially for small, slowly flying bats. To the extent that unsteady phenomena are important in the generation of the aerodynamic forces of bat flight [Cantwell and Coles, 1983; Boratav et al., 1992; Zabusky et al., 1995], we will remain severely limited in our ability to interpret the functional and evolutionary significance of the structural design of wings until we broaden our understanding of the mechanistic bases of bat flight. Fortunately, experimental fluid dynamics approaches, including use of particle image velocimetry, are now being applied to the study of bird and bat flight as well [Spedding et al., 2003; Warrick et al., 2005; Tian et al., 2006; Hedenström et al., 2007], revealing patterns of air velocities in the wakes near flying vertebrates, and producing detailed pictures of flight dynamics that promise new insights into bat and bird flight. These studies demonstrate that it is possible to analyze the structure of the flow in the wakes of flying vertebrates, and to calculate mechanical and energetic quantities directly from the wake 'footprint'. Over the next 10–20 years, we expect that we will be able to understand the biomechanics of the bat skeleton in new and functionally relevant ways, and to integrate the disparate lines of research that contribute to our understanding of bat biology and evolution.

Acknowledgements

We are grateful to individuals and agencies who have supported this work over the last 10 years: the National Science Foundation, the Air Force Office of Scientific Research, monitored by Drs. R. Jeffries and W. Larkin, the Brown University UTRA program, the Brown University Salomon Fund, the Lubee Bat Conservancy, the Concord Field Station of Harvard University and the University of Queensland. We thank Ted Garland for providing software for phylogenetic comparisons and answering our numerous questions. Our experimental work and thinking have benefited from our interactions with: Michael Bennett, Andy Biewener, Kenny Breuer, Dave Carrier, Jennifer Gray Chickering, Pepe Iriarte, Les Hall, Ty Hedrick, Tom Kunz, Helen Papadimitriou, Antigone Parker Parrish, Dan Riskin, Arnold Song, Allyson Walsh and David Willis.

References

Adams, R.A. (1992a) Comparative skeletogenesis of the forearm of the little brown bat *(Myotis lucifugus)* and the Norway rat *(Rattus norvegicus)*. J Morphol *214:* 251–260.

Adams, R.A. (1992b) Stages of development and sequence of bone formation in the little brown bat, *Myotis lucifugus*. J Mammal *73:* 160–167.

Adams, R.A. (1998) Evolutionary implications of developmental and functional integration in bat wings. J Zool Lond *246:* 164–174.

Akaike, H. (1974) A new look at the statistical model identification. IEEE Trans Autom Control *19:* 716–723.

Altenbach, S.J. (1979) Locomotor morphology of the vampire bat, *Desmodus rotundus*. Spec Pub Am Soc Mammal *6:* 1–133.

Barbier, A., C. Martel, M.C. de Vernejoul, F. Tirode, M. Nys, G. Mocaer, C. Morieux, H. Murakami, F. Lacheretz (1999) The visualization and evaluation of bone architecture in the rat using three-dimensional X-ray microcomputed tomography. J Bone Miner Metab *17:* 37–44.

Benjamini, Y., Y. Hochberg (1995) Controlling the false discovery rate – A practical and powerful approach to multiple testing. J R Stat Soc Ser B Methodol *57:* 289–300.

Biewener, A.A. (1992) In vivo measurement of bone strain and tendon force; in Biewener, A.A. (ed): Biomechanics: A Practical Approach. Oxford, Oxford University Press, vol 2: Structures, pp 123–147.

Biewener, A.A. (1993) Safety factors in bone strength. Calc Tissue Int *53:* S68–S74.

Biewener, A.A., J.E.A. Bertram (1993) Skeletal strain patterns in relation to exercise training during growth. J Exp Biol *185:* 51–69.

Biewener, A.A., K.P. Dial (1995) In vivo strain in the humerus of pigeons *(Columba livia)* during flight. J Morphol *225:* 61–75.

Biewener, A.A., J. Thomason, L.E. Lanyon (1983) Mechanics of locomotion and jumping in the forelimb of the horse *Equus*: in vivo stress developed in the radius and metacarpus. J Zool Lond *201:* 67–82.

Birch, J.M., M.H. Dickinson (2001) Spanwise flow and the attachment of the leading-edge vortex on insect wings. Nature *412:* 729–733.

Birt, P., L.S. Hall, G.C. Smith (1997) Ecomorphology of the tongues of Australian Megachiroptera (Chiroptera: Pteropodidae). Aust J Zool *45:* 369–384.

Blomberg, S.P., T. Garland, A.R. Ives (2003) Testing for phylogenetic signal in comparative data: behavioral traits are more labile. Evolution *57:* 717–745.

Bohr, H., O. Schaadt (1985) Bone-mineral content of the femoral-neck and shaft – Relation between cortical and trabecular bone. Calcif Tissue Int *37:* 340–344.

Borah, B., T.E. Dufresne, M.D. Cockman, G.J. Gross, E.W. Sod, W.R. Myers, K.S. Combs, R.E. Higgins, S.A. Pierce, M.L. Stevens (2000) Evaluation of changes in trabecular bone architecture and mechanical properties of minipig vertebrae by three-dimensional magnetic resonance microimaging and finite element modeling. J Bone Miner Res *15:* 1786–1797.

Boratav, O.N., R.B. Pelz, N.J. Zabusky (1992) Reconnection in orthogonally interacting vortex tubes: direct numerical simulations and quantifications. Phys Fluids A *4:* 581–605.

Burnham, K.P., D. Anderson (2002) Model Selection and Multi-Model Inference: A Practical Information-Theoretic Approach. Secaucus, Springer.

Butler, M.A., A.A. King (2004) Phylogenetic comparative analysis: a modeling approach for adaptive evolution. Am Nat *164:* 683–695.

Cantwell, B.J., D. Coles (1983) An experimental study of entrainment and transport in the turbulent near wake of a circular cylinder. J Fluid Mech *136:* 321–374.

Carrier, D.R. (1983) Postnatal ontogeny of the musculo-skeletal system in the black-tailed jack rabbit *(Lepus californicus)*. J Zool Lond *201:* 27–55.

Carter, D.R. (1978) Anisotropic analysis of strain rosette information from cortical bone. J Biomech *11:* 199–202.

Carter, D.R., D.J. Smith, D.M. Spengler, C.H. Daly, V.H. Frankel (1980) Measurement and analysis of in vivo bone strain in the canid radius and ulna. J Biomech *13:* 27–38.

Chen, X., J. Yan, A.M. Karlsson (2006) On the determination of residual stress and mechanical properties by indentation. Mat Sci Eng A Struct *416:* 139–149.

Chickering, J.G. (1995) Scaling of Skeletal Adaptation, Locomotor Performance and Muscular Morphology in Sciurids (Mammalia: Rodentia); PhD dissertation, Brown University.

Chickering, J.G., A.J. Sokoloff (1996) Innervation of propatagial musculature in a flying squirrel, *Glaucomys volans* (Rodentia, Sciuridae). Brain Behav Evol *47:* 1–7.

Coleman, J.C., R.T. Hart, I. Owen, Y. Tankano, D.B. Burr (2002) Characterization of dynamic three-dimensional strain fields in the canine radius. J Biomech *35:* 1677–1683.

Combes, S.A., T.L. Daniel (2003) Flexural stiffness in insect wings. II. Spatial distribution and dynamic wing bending. J Exp Biol *206:* 2989–2997.

Cowin, S.C. (1989) A resolution restriction for Wolff's law of trabecular architecture. Bull Hosp J Dis Orth Inst *49:* 205–212.

Crowley, G.V., L.S. Hall (1994) Histological observations on the wing of the grey-headed flying fox *(Pteropus poliocephalus)* (Chiroptera: Pteropodidae). Aust J Zool *42:* 215–236.

Curran-Everett, D. (2000) Multiple comparisons: philosophies and illustrations. Am J Phys R *279:* R1–R8.

Currey, J.D. (1984) The Mechanical Adaptations of Bones. Princeton, Princeton University Press.

Currey, J.D. (2002) Bones: Structure and Mechanics. Princeton, Princeton University Press.

Currey, J.D. (2003) The many adaptations of bone. J Biomech *36:* 1487–1495.

Daniel, T.L., S.A. Combes (2002) Flexible wings and fins: bending by inertial or fluid-dynamic forces? Int Comp Biol *42:* 1044–1049.

Demes, B., J.T. Stern, M.R. Hausman, S.G. Larson, K.J. McLeod, C.T. Rubin (1998) Patterns of strain in the macaque ulna during functional activity. Am J Phys Anthropol *106:* 87–100.

Dial, K.P. (2003) Wing-assisted incline running and the evolution of flight. Science *299:* 402–404.

Dickinson, M.H. (2000) The structure and function of flight trajectories in freely flying fruit flies. Am Zool *40:* 999–999.

Dickinson, M.H., F.O. Lehmann, S.P. Sane (1999) Wing rotation and the aerodynamic basis of insect flight. Science *284:* 1954–1960.

Dong, X.N., X.E. Guo (2004) The dependence of transversely isotropic elasticity of human femoral cortical bone on porosity. J Biomech *37:* 1281–1287.

Dumont, E.R., J. Piccirillo, L.R. Grosse (2005) Finite-element analysis of biting behavior and bone stress in the facial skeletons of bats. Anat Rec A *283A:* 319–330.

Dumont, E.L., S.M. Swartz (in press) Biomechanical approaches and ecological research; in Kunz, T.H., S. Parsons (eds): Ecological and Behavioral Methods for the Study of Bats. Baltimore, Johns Hopkins University Press.

Eaton, T.H. (1944) Modifications of the shoulder girdle related to reach and stride in mammals. J Morphol *75:* 167–171.

Eisenberg, J.F. (1981) The Mammalian Radiations: An Analysis of Trends in Evolution, Adaptation, and Behavior. Chicago, University of Chicago Press.

Eisenberg, J.F. (1989) Mammals of the Neotropics. Chicago, University of Chicago Press, vol 1: The northern neotropics: Panama, Colombia, Venezuela, Guyana, Surinam, French Guiana.

Ellington, C.P. (1984) The aerodynamics of hovering insect flight. IV. Aerodynamic mechanisms. Philos Trans R Soc Lond B *305:* 1–15.

Ellington, C.P., C. Van den Berg, A.P. Willmott, A.L.R. Thomas (1996) Leading-edge vortices in insect flight. Nature *384:* 626–630.

Ennos, A.R. (1995) Mechanical-behavior in torsion of insect wings, blades of grass and other cambered structures. Proc R Soc Lond B *259:* 15–18.

Erickson, G.M., J. Catanese, T.M. Keaveny (2002) Evolution of the biomechanical material properties of the femur. Anat Rec *268:* 115–124.

Feldkamp, L.A., S.A. Goldstein, A.M. Parfitt, G. Jesion, M. Kleerekoper (1989) The direct examination of 3-dimensional bone architecture in vitro by computed-tomography. J Bone Miner Res *4:* 3–11.

Felsenstein, J. (1985) Phylogenies and the comparative method. Am Nat *125:* 1–15.

Felsenstein, J. (1988a) Evolution – Perils of molecular introspection. Nature *335:* 118–118.

Felsenstein, J. (1988b) Phylogenies and quantitative characters. Annu Rev Ecol Syst *19:* 445–471.

Felsenstein, J. (1988c) Phylogenies from molecular sequences – Inference and reliability. Annu Rev Genet *22:* 521–565.

Field, J.S., M.V. Swain, R.D. Dukino (2003) Determination of fracture toughness from the extra penetration produced by indentation-induced pop-in. J Mater Res *18:* 1412–1419.

Gao, H.J. (2006) Application of fracture mechanics concepts to hierarchical biomechanics of bone and bone-like materials. Int J Fract *138:* 101–137.

Garland, T. Jr., A.W. Dickerman, C.M. Janis, J.A. Jones (1993) Phylogenetic analysis of covariance by computer-simulation. Syst Biol *42:* 265–292.

Garland, T. Jr., P.H. Harvey, A.R. Ives (1992) Procedures for the analysis of comparative data using phylogenetically independent contrasts. Syst Biol *41:* 18–32.

Garland, T. Jr., A.R. Ives (2000) Using the past to predict the present: confidence intervals for regression equations in phylogenetic comparative methods. Am Nat *155:* 346–364.

Garland, T. Jr., P.E. Midford, A.R. Ives (1999) An introduction to phylogenetically based statistical methods, with a new method for confidence intervals on ancestral values. Am Zool *39:* 374–388.

Goodwin, K.J., N.A. Sharkey (2002) Material properties of interstitial lamellae reflect local strain environments. J Orthop Res *20:* 600–606.

Hansen, T.F., E.P. Martins (1996) Translating between microevolutionary process and macroevolutionary patterns: the correlation structure of interspecific data. Evolution *50:* 1404–1417.

Harvey, P.H., M.D. Pagel (1991) The Comparative Method in Evolutionary Biology. Oxford, Oxford University Press.

Hedenström, A., L.C. Johansson, M. Wolf, R. von Busse, Y. Winter, G.R. Spedding (2007) Bat flight generates complex aerodynamic tracks. Science *316:* 894–897.

Hedrick, T.L. (2003) Low-speed maneuvering flight in the rose-breasted cockatoo. Int Comp Biol *43:* 822–822.

Hedrick, T.L., J.R. Usherwood, A.A. Biewener (2004) Wing inertia and whole-body acceleration: an analysis of instantaneous aerodynamic force production in cockatiels *(Nymphicus hollandicus)* flying across a range of speeds. J Exp Biol *207:* 1689–1702.

Hengsberger, S., A. Kulik, P. Zysset (2002) Nanoindentation discriminates the elastic properties of individual human bone lamellae under dry and physiological conditions. Bone *30:* 178–184.

Howell, D.J., J. Pylka (1977) Why bats hang upside down: a biomechanical hypothesis. J Theor Biol *69:* 625–631.

Ives, A.R., P.E. Midford, T. Garland Jr. (2007) Within-species variation and measurement error in phylogenetic comparative methods. Syst Biol *56:* 252–270.

Jenkins, F.A. (1974) The movement of the shoulder in claviculate and aclaviculate mammals. J Morphol 144: 71–84.

Ji, B.H., H.J. Gao (2004) Mechanical properties of nanostructure of biological materials. J Mech Phys Solids *52:* 1963–1990.

Ji, B.H., H.J. Gao (2006) Elastic properties of nanocomposite structure of bone. Comp Sci Tech *66:* 1212–1218.

Kim, J.Y., S.H. Kim, J.S. Lee, K.W. Lee, D. Kwon (2006) Mechanical characterization of nanostructured materials using nanoindentation. Methods Mater Int *12:* 219–223.

Kunz, T.H., S.K. Robson (1995) Postnatal-growth and development in the Mexican free-tailed bat *(Tadarida brasiliensis mexicana)* – Birth size, growth-rates, and age estimation. J Mammal *76:* 769–783.

Kurian, D.C. (1993) Allometric Relationships of Limb Bones in the Smallest Terrestrial Mammals; Senior Undergraduate Honors thesis, Brown University.

La Barbera, M. (1989) Analyzing body size as a factor in ecology and evolution. Annu Rev Ecol Syst *20:* 97–118.

Laib, A., O. Barou, L. Vico, M.H. Lafage-Proust, C. Alexandre, P. Ruegsegger (2000) 3d micro-computed tomography of trabecular and cortical bone architecture with application to a rat model of immobilisation osteoporosis. Med Biol Eng Comp *38:* 326–332.

Levin, O., W. Shyy (2001) Optimization of a low Reynolds number airfoil with flexible membrane. CMES Comp Mod Eng Sci *2:* 523–536.

Li, X.D., B. Bhushan (2002) A review of nanoindentation continuous stiffness measurement technique and its applications. Mater Charact *48:* 11–36.

Lian, Y.S., W. Shyy, D. Viieru, B.N. Zhang (2003) Membrane wing aerodynamics for micro air vehicles. Prog Aerospace Sci *39:* 425–465.

Ma, D.J., T.H. Zhang, C.W. Ong (2006) Evaluation of the effectiveness of representative methods for determining Young's modulus and hardness from instrumented indentation data. J Mater Res *21:* 225–233.

Maddison, W.P., D.R. Maddison (2006) Mesquite: a modular system for evolutionary analysis. Version 1.12. http://mesquiteproject.org.

Martins, E.P., J.A.F. Diniz, E.A. Housworth (2002) Adaptive constraints and the phylogenetic comparative method: a computer simulation test. Evolution *56:* 1–13.

Martins, E.P., E.A. Housworth (2002) Phylogeny shape and the phylogenetic comparative method. Syst Biol *51:* 873–880.

Mikić, B., D.R. Carter (1995) Bone strain-gauge data and theoretical-models of functional adaptation. J Biomech *28:* 465–469.

Mulder, L., J.H. Koolstra, T. Van Euden (2004) Accuracy of microCT in the quantitative determination of the degree and distribution of mineralization in developing bone. Acta Radiol *45:* 769–777.

Müller, U.K., E.J. Stamhuis, C.P. Ellington (2000) Quantifying the leading-edge vortex of a hovering robotic insect during the downstroke. Am Zool *40:* 1142–1143.

Murphy, W.J., E. Eizirik, S.J. O'Brien, O. Madsen, M. Scally, C.J. Douady, E. Teeling, O.A. Ryder, M.J. Stanhope, W.W. de Jong, M.S. Springer (2001) Resolution of the early placental mammal radiation using bayesian phylogenetics. Science *294:* 2348–2351.

Norberg, U.M. (1970) Functional osteology and myology of the wing of *Plecotus auritus* Linnaeus (Chiroptera). Ark Zool *22:* 483–543.

Norberg, U.M. (1972) Functional osteology and myology of the wing of the dog-faced bat *Rousettus aegyptiacus* (É. Geoffroy) (Pteropodidae). Z Morphol Tiere *73:* 1–44.

Norberg, U.M. (1981) Allometry of bat wings and legs and comparisons with bird wings. Philos Trans R Soc Lond B *292:* 359–398.

Norberg, U.M. (1990) Vertebrate Flight: Mechanics, Physiology, Morphology, Ecology and Evolution. Berlin, Springer-Verlag.

Norberg, U.M.L., Y. Winter (2006) Wing beat kinematics of a nectar-feeding bat, *Glossophaga soricina*, flying at different flight speeds and Strouhal numbers. J Exp Biol *209:* 3887–3897.

Nowak, R.M. (ed) (1991) Walker's Mammals of the World, ed 5. Baltimore, Johns Hopkins University Press.

Orso, S., U.G.K. Wegst, E. Arzt (2006) The elastic modulus of spruce wood cell wall material measured by an in situ bending technique. J Mater Sci *41:* 5122–5126.

Page, K.M. (1982) Bone and the preparation of bone sections; in Bancroft, J.D., A. Stevens (eds): Theory and Practice of Histological Techniques. Edinburgh, Churchill Livingstone, pp 297–331.

Pagel, M.D. (1992) A method for the analysis of comparative data. J Theor Biol *156:* 431–442.

Papadimitriou, H.M., S.M. Swartz, T.H. Kunz (1996) Ontogenetic and anatomic variation in mineralization of the wing skeleton of the Mexican free-tailed bat, *Tadarida brasiliensis*. J Zool *240:* 411–426.

Radovic, M., E. Lara-Curzio, L. Riester (2004) Comparison of different experimental techniques for determination of elastic properties of solids. Mater Sci Eng A Struct *368:* 56–70.

Ramamurti, R., W.C. Sandberg (2002) A three-dimensional computational study of the aerodynamic mechanisms of insect flight. J Exp Biol *205:* 1507–1518.

Rayner, J.M.V. (1985) Linear relations in biomechanics: the statistics of scaling functions. J Zool Lond A *206:* 415–439.

Rayner, J.M.V., G. Jones, A. Thomas (1986) Vortex flow visualizations reveal change in upstroke function with flight speed in bats. Nature *321:* 162–164.

Rho, J.Y., J.D. Currey, P. Zioupos, G.M. Pharr (2001) The anisotropic Young's modulus of equine secondary osteones and interstitial bone determined by nanoindentation. J Exp Biol *204:* 1775–1781.

Rice, W.R. (1989) Analyzing tables of statistical tests. Evolution *43:* 223–225.

Riskin, D.K., J.E.A. Bertram, J.W. Hermanson (2005) Testing the hind limb-strength hypothesis: non-aerial locomotion by Chiroptera is not constrained by the dimensions of the femur or tibia. J Exp Biol *208:* 1309–1319.

Riskin, D.K., S. Parsons, W.A. Schutt, G.G. Carter, J.W. Hermanson (2006) Terrestrial locomotion of the New Zealand short-tailed bat *Mystacina tuberculata* and the common vampire bat *Desmodus rotundus.* J Exp Biol *209:* 1725–1736.

Ruegsegger, P., B. Koller, R. Müller (1996) A microtomographic system for the nondestructive evaluation of bone architecture. Calcif Tissue Int *58:* 24–29.

Sane, S.P., M.H. Dickinson (2002) The aerodynamic effects of wing rotation and a revised quasi-steady model of flapping flight. J Exp Biol *205:* 1087–1096.

Schenk, R.K., A.J. Olah, W. Herrmann (1984) Preparation of calcified tissues for light microscopy; in Dickson, G.R. (ed): Methods of Calcified Tissue Preparation. Amsterdam, Elsevier, pp 1–56.

Scholz, T., G.A. Schneider, J. Munoz-Saldana, M.V. Swain (2004) Fracture toughness from submicron derived indentation cracks. Appl Phys Lett *84:* 3055–3057.

Schutt, W.A. (1993) Digital morphology in the Chiroptera – The passive digital lock. Acta Anat *148:* 219–227.

Schutt, W.A., J.S. Altenbach, Y.H. Chang, D.M. Cullinane, J.W. Hermanson, F. Muradali, J.E.A. Bertram (1997) The dynamics of flight-initiating jumps in the common vampire bat *Desmodus rotundus.* J Exp Biol *200:* 3003–3012.

Schutt, W.A., N.B. Simmons (2001) Morphological specializations of *Cheiromeles* (naked bulldog bats; Molossidae) and their possible role in quadrupedal locomotion. Acta Chiropterol *3:* 225–235.

Sears, K.E., R.R. Behringer, J.J. Rasweiler, L.A. Niswander (2006) Development of bat flight: morphologic and molecular evolution of bat wing digits. Proc Natl Acad Sci USA *103:* 6581–6586.

Shyy, W., M. Berg, D. Ljungqvist (1999a) Flapping and flexible wings for biological and micro air vehicles. Prog Aerospace Sci *35:* 455–505.

Shyy, W., F. Klevebring, M. Nilsson, J. Sloan, B. Carroll, C. Fuentes (1999b) Rigid and flexible low Reynolds number airfoils. J Aircr *36:* 523–529.

Silva, M., J.A. Downing (1995) Handbook of Mammalian Body Masses. Boca Raton, CRC Press.

Simmons, N.B., T.H. Quinn (1994) Evolution of the digital tendon locking mechanism in bats and dermopterans: a phylogenetic perspective. J Mammal Evol *2:* 231–254.

Smith, R., W. Shyy (1996) Computation of aerodynamic coefficients for a flexible membrane airfoil in turbulent flow: a comparison with classical theory. Phys Fluids *8:* 3346–3353.

Solloway, M.J., A.T. Dudley, E.K. Bikoff, K.M. Lyons, B.L.M. Hogan, E.J. Robertson (1998) Mice lacking *Bmp6* function. Dev Genet *22:* 321–339.

Spedding, G.R., A. Hedenström, M. Rosén (2003) A family of vortex wakes generated by a thrush nightingale in free flight over its entire range of flight speeds. J Exp Biol *206:* 2313–2344.

Springer, M.S., M.J. Stanhope, O. Madsen, W.W. de Jong (2004) Molecules consolidate the placental mammal tree. Trends Ecol Evol *19:* 430–438.

Springer, M.S., E.C. Teeling, O. Madsen, M.J. Stanhope, W.W. de Jong (2001) Integrated fossil and molecular data reconstruct bat echolocation. Proc Natl Acad Sci USA *98:* 6241–6246.

Storey, J.D. (2002) A direct approach to false discovery rates. J R Stat Soc B *64:* 479–498.

Storey, J.D., R. Tibshirani (2003) Statistical significance for genomewide studies. Proc Natl Acad Sci USA *100:* 9440–9445.

Swartz, S.M. (1991) Strain analysis as a tool for functional morphology. Am Zool *31:* 655–669.

Swartz, S.M. (1997) Allometric patterning in the limb skeleton of bats: implications for the mechanics and energetics of powered flight. J Morphol *234:* 277–294.

Swartz, S.M. (1998) Skin and bones: the mechanical properties of bat wing tissues; in Kunz, T.H., P.A. Racey (eds): Bats: Phylogeny, Morphology, Echolocation, and Conservation Biology. Washington, Smithsonian Institution Press, pp 109–126.

Swartz, S.M., M.B. Bennett, D.R. Carrier (1992) Wing bone stresses in free flying bats and the evolution of skeletal design for flight. Nature *359:* 726–729.

Swartz, S.M., K.L. Bishop, M.-F. Ismael-Aguirre (2005) Dynamic complexity of wing form in bats: implications for flight performance; in Akbar, Z., G. McCracken, T.H. Kunz (eds): Functional and Evolutionary Ecology of Bats. Oxford, Oxford University Press.

Swartz, S.M., P.W. Freeman, E.F. Stockwell (2003) Ecomorphology; in Kunz, T.H., M.B. Fenton (eds): Bat Ecology. Chicago, University of Chicago Press, pp 257–300.

Swartz, S.M., M.D. Groves, H.D. Kim, W.R. Walsh (1996) Mechanical properties of bat wing membrane skin. J Zool Lond *239:* 357–378.

Teeling, E.C., O. Madsen, R.A. Van den Bussche, W.W. de Jong, M.J. Stanhope, M.S. Springer (2002) Microbat paraphyly and the convergent evolution of a key innovation in old world rhinolophoid microbats. Proc Natl Acad Sci USA *99:* 1431–1436.

Teeling, E.C., M.S. Springer, O. Madsen, P. Bates, S.J. O'Brien, W.J. Murphy (2005) A molecular phylogeny for bats illuminates biogeography and the fossil record. Science *307:* 580–584.

Thewissen, J.G.M., S.K. Babcock (1991) Distinctive cranial and cervical innervation of wing muscles – New evidence for bat monophyly. Science *251:* 934–936.

Tian, X., J. Iriarte-Diaz, K. Middleton, R. Galvao, E. Israeli, A. Roemer, A. Sullivan, A. Song, S. Swartz, K.S. Breuer (2006) Direct measurements of the kinematics and dynamics of bat flight. Bioinsp Biomim *1:* S10–S18.

Turner, C.H., J. Rho, Y. Takano, T.Y. Tsui, G.M. Pharr (1999) The elastic properties of trabecular and cortical bone tissues are similar: results from two microscopic measurement techniques. J Biomech *32:* 437–441.

Tytell, E.D., C.P. Ellington (2000) The vortex wake of the hawkmoth, *Manduca sexta*: simulation and Reynolds number effects. Am Zool *40:* 1241–1241.

Unwin, D.M. (1999) Pterosaurs: back to the traditional model? Trends Ecol Evol *14:* 263–268.

Unwin, D.M., N.N. Bakhurina (1994) *Sordes pilosus* and the nature of the pterosaur flight apparatus. Nature *371:* 62–64.

Usherwood, J.R., T.L. Hedrick, C.P. McGowan, A.A. Biewener (2005) Dynamic pressure maps for wings and tails of pigeons in slow, flapping flight, and their energetic implications. J Exp Biol *208:* 355–369.

Van den Berg, C., C.P. Ellington (1997a) The three-dimensional leading-edge vortex of a 'hovering' model hawkmoth. Philos Trans R Soc B *352:* 329–340.

Van den Berg, C., C.P. Ellington (1997b) The vortex wake of a 'hovering' model hawkmoth. Philos Trans R Soc B *352:* 317–328.

Vandoros, J.D., E.R. Dumont (2004) Use of the wings in manipulative and suspensory behaviors during feeding by frugivorous bats. J Exp Zool A *301A:* 361–366.

Van Landingham, M.R. (2003) Review of instrumented indentation. J Res Natl Inst Stand Tech *108:* 249–265.

Vaughan, T.A. (1959) Functional morphology of three bats: *Eumops, Myotis, Macrotus.* Univ Kansas Publ Mus Nat Hist *12:* 1–153.

Vaughan, T.A. (1970a) The muscular system; in Wimsatt, W.A. (ed): The Biology of Bats. New York, Academic Press, pp 140–194.

Vaughan, T.A. (1970b) The skeletal system; in Wimsatt, W.A. (ed): The Biology of Bats. New York, Academic Press, pp 98–139.

Wang, X.M., F.Z. Cui, J. Ge, Y. Zhang, C. Ma (2002) Variation of nanomechanical properties of bone by gene mutation in the zebrafish. Biomaterials *23:* 4557–4563.

Warrick, D.R., B.W. Tobalske, D.R. Powers (2005) Aerodynamics of the hovering hummingbird. Nature *435:* 1094–1097.

Warton, D.I., I.J. Wright, D.S. Falster, M. Westoby (2006) Bivariate line-fitting methods for allometry. Biol Rev *81:* 259–291.

Wilkinson, M.T. (2007) Sailing the skies: the improbable aeronautical success of the pterosaurs. J Exp Biol *210:* 1663–1671

Wilkinson, M.T., D.M. Unwin, C.P. Ellington (2006) High lift function of the pteroid bone and forewing of pterosaurs. Proc R Soc B Biol Sci *273:* 119–126.

Willmott, A.P., C.P. Ellington, A.L.R. Thomas (1997) Flow visualization and unsteady aerodynamics in the flight of the hawkmoth, *Manduca sexta.* Philos Trans R Soc B *352:* 303–316.

Wootton, R.J. (1993) Leading-edge section and asymmetric twisting in the wings of flying butterflies (Insecta, Papilionoidea). J Exp Biol *180:* 105–117.

Yoshikawa, T., S. Mori, A.J. Santiesteban, T.C. Sun, E. Hafstad, J. Chen, D.B. Burr (1994) The effects of muscle fatigue on bone strain. J Exp Biol *188:* 217–233.

Zabusky, N.J., V.M. Fernandez, D. Silver (1995) Collapse, intensification, and reconnection in vortex dominated flows: visiometrics and modeling. Physica D 86*:* 1–11.

Ziv, V., H.D. Wagner, S. Weiner (1996) Microstructure-microhardness relations in parallel-fibered and lamellar bone. Bone *18:* 417–428.

Zook, J. (in press) Somatosensory adaptations of flying mammals; in Kaas, J.H., L. Krubitzer (eds): Evolution of Nervous Systems. Elsevier.

Zook, J.M. (2005) The neuroethology of touch in bats: cutaneous receptors of the bat wing. Neurosci Abstr *78:* 21.

Zook, J.M., B.C. Fowler (1986) A specialized mechanoreceptor array of the bat wing. Myotis *23–24:* 31–36.

Zysset, P.K., X.E. Guo, C.E. Hoffler, K.E. Moore, S.A. Goldstein (1999) Elastic modulus and hardness of cortical and trabecular bone lamellae measured by nanoindentation in the human femur. J Biomech *32:* 1005–1012.